

# Effective one body multipolar waveform model for spin-aligned, quasi-circular, eccentric, hyperbolic black hole binaries.

Alessandro Nagar<sup>2,3</sup>, Alice Bonino<sup>1</sup>, and Piero Rettegno<sup>1,2</sup>

<sup>1</sup> *Dipartimento di Fisica, Università di Torino, via P. Giuria 1, 10125 Torino, Italy*

<sup>2</sup> *INFN Sezione di Torino, Via P. Giuria 1, 10125 Torino, Italy and*

<sup>3</sup> *Institut des Hautes Etudes Scientifiques, 91440 Bures-sur-Yvette, France*

(Dated: February 2, 2022)

Building upon recent work, we present an improved effective-one-body (EOB) model for spin-aligned, coalescing, black hole binaries with generic orbital configurations, i.e. quasi-circular, eccentric or hyperbolic orbits. The model, called **TEOBResumSGeneral**, relies on the idea of incorporating general Newtonian prefactors, instead of the usual quasi-circular ones, in both radiation reaction and waveform. The major advance with respect to previous work is that the quasi-circular limit of the model is now correctly informed by numerical relativity (NR) quasi-circular simulation. This provides EOB/NR unfaithfulness for the dominant quadrupolar waveform, calculated with Advanced LIGO noise, at most of the order of 1% over a meaningful portion of the quasi-circular NR simulations computed by the Simulating eXtreme Spacetime (SXS) collaboration. In the presence of eccentricity, the model is similarly NR-faithful,  $\lesssim 1\%$ , all over the 28 public SXS NR datasets, with initial eccentricity up to  $\simeq 0.2$ , mass ratio up to  $q = 3$  and dimensionless spin magnitudes as large as  $+0.7$ . Higher multipoles, up to  $\ell = 5$  are also reliably modeled through the eccentric inspiral, plunge, merger and ringdown. For hyperbolic-like configurations, we also show that the EOB computed scattering angle is in excellent agreement with all currently available NR results.

Keywords:

## I. INTRODUCTION

A recent work [1] introduced an effective one body (EOB) waveform model for spin-aligned, eccentric, black hole binaries. This waveform model is not limited to stable configurations, but can also generate waveforms for hyperbolic encounters and dynamical captures from binary black holes (BBHs) coalescences [2]. The pivotal technical aspect behind this waveform model is the possibility of accurately generalizing the EOB resummed quasi-circular radiation reaction (and waveform) to generic orbits by simply considering generic (i.e., non quasi-circular) Newtonian prefactors in these functions. In order to assess the quality of the model, Ref. [1] compared the so constructed EOB waveforms to 22 eccentric numerical relativity (NR) public waveforms from the SXS catalog [3–15]. The comparison was performed by computing the EOB/NR unfaithfulness (or mismatch) using the Advanced LIGO power spectral density. For the model of Ref. [1] this led to unfaithfulnesses that reached up to 3%. Although this result could be considered satisfactory at the time, the model of Ref. [1] was not especially optimized and can be improved along several directions. In particular, it relied on the EOB conservative dynamics of Refs. [16, 17], that was NR-informed using the *standard quasi-circular* EOB radiation reaction. The model of Refs. [16, 17], called **TEOBiResumS<sub>SM</sub>**, incorporates higher-order modes and is the most advanced and accurate version of the **TEOBResumS** model [18]. To simplify the nomenclature, from now on we address as **TEOBResumS** the model of Ref. [17]. The purpose of this paper is to correct the inconsistency of Refs. [2, 16], by determining new NR-informed EOB flexibility functions ( $a_6^c, c_3$ ) [16, 17], consistent with the general, non quasi-

circular, radiation reaction and waveform. We will see that this modification is sufficient to lower the EOB/NR unfaithfulness in the eccentric sector at approximately the 1% level. To distinguish it from the quasi-circular model **TEOBResumS**, and since it can deal also with general, spin-aligned, configurations, like hyperbolic scattering or capture, for convenience we will address it as **TEOBResumSGeneral**. The paper is organized as follows. In Sec. II we recall the structure of the EOB dynamics and waveform, provide the new expressions of ( $a_6^c, c_3$ ) and illustrate the related new EOB/NR waveform performance for quasi-circular configurations. The eccentric case is discussed in Sec. III, while Sec. IV provides a new EOB/NR comparison of the scattering angle. Our findings are summarized in Sec. V. Throughout this paper we mostly use geometric units with  $G = c = 1$ .

## II. QUASI-CIRCULAR CONFIGURATIONS

### A. Effective one body dynamics

The structure of the dynamics of the EOB eccentric model is essentially the same discussed in Sec. II of Ref. [1] and thus we limit ourselves to report here the few details that we have improved on. We adopt the usual notation within the EOB formalism. We use mass-reduced phase-space variables ( $r, \varphi, p_\varphi, p_{r_*}$ ), related to the physical ones by  $r = R/M$  (relative separation),  $p_{r_*} = P_{R_*}/\mu$  (radial momentum),  $p_\varphi = P_\varphi/(\mu M)$  (angular momentum) and  $t = T/M$  (time), where  $\mu \equiv m_1 m_2 / M$  and  $M \equiv m_1 + m_2$ . The radial momentum is  $p_{r_*} \equiv (A/B)^{1/2} p_r$ , where  $A$  and  $B$  are the EOB potentials (with included spin-spin interactions [19]). The EOB Hamilto-

nian is  $\hat{H}_{\text{EOB}} \equiv H_{\text{EOB}}/\mu = \nu^{-1}\sqrt{1 + 2\nu(\hat{H}_{\text{eff}} - 1)}$ , with  $\nu \equiv \mu/M$  and  $\hat{H}_{\text{eff}} = \tilde{G}p_\varphi + \hat{H}_{\text{eff}}^{\text{orb}}$ , where  $\tilde{G}p_\varphi$  incorporates odd-in-spin (spin-orbit) effects while  $\hat{H}_{\text{eff}}^{\text{orb}}$  incorporates even-in-spin effects [18]. We denote dimensionless spin variables as  $\chi_i \equiv S_i/m_i^2$ , and adopt  $\hat{\mathcal{F}}_{\varphi,r} \equiv \mathcal{F}_{\varphi,r}/\mu$  as  $\mu$ -rescaled radiation reaction forces. The novelties here mainly pertain the analytical expressions ( $\hat{\mathcal{F}}_\varphi, \hat{\mathcal{F}}_r$ ) and thus impact the related Hamilton's equations, that we rewrite for completeness:

$$\dot{p}_\varphi = \hat{\mathcal{F}}_\varphi, \quad (1)$$

$$\dot{p}_{r_*} = \sqrt{\frac{A}{B}} \left( -\partial_r \hat{H}_{\text{EOB}} + \hat{\mathcal{F}}_r \right). \quad (2)$$

As mentioned in the introduction, the dynamics also depends on two effective EOB flexibility functions that are informed by NR simulations; i.e., the 4.5PN spin-orbit effective function  $c_3(\nu, \chi_1, \chi_2)$ , that enters  $\tilde{G}$ , and the effective 5PN function  $a_6^c(\nu)$ , that enters the Padé resummed radial potential  $A(r)$ . Reference [1] used a generic, 2PN accurate, expression of  $\hat{\mathcal{F}}_r$ , resummed by taking its inverse. Instead,  $(a_6^c, c_3)$  were the same of the standard quasi-circular model of Ref. [2]. Such a choice, done for simplicity at the time, is an evident source of systematic errors in the waveform model. It was already pointed out in Ref. [1] that it would be necessary to use quasi-circular NR simulations to NR-inform two *new* functions  $(a_6^c, c_3)$  to be compatible with the general expressions for  $(\hat{\mathcal{F}}_\varphi, \hat{\mathcal{F}}_r)$  and with the corresponding waveform. This is our scope here, but in doing so we also modify *both* the analytical expressions of  $(\hat{\mathcal{F}}_\varphi, \hat{\mathcal{F}}_r)$  with respect to Ref. [1]. For what concerns  $\hat{\mathcal{F}}_\varphi$ , the simplifying choice of [1] of incorporating noncircular corrections with  $\ell = m = 2$  overall factor also introduces some systematics, since the subdominant flux modes are multiplied by an incorrect noncircular Newtonian factor. Here we go beyond the previous, simplified, approach and we incorporate the noncircular correction, Eq. (7) of [1], as a multiplicative factor entering *only* the  $\ell = m = 2$  flux contribution<sup>1</sup>. In addition, while performing the EOB/NR comparison with quasi-circular data aimed at determining a consistent expression of  $a_6^c(\nu)$ , we realized that the general, 2PN resummed, expression for  $\hat{\mathcal{F}}_r$  used in [1] reduces the flexibility of the quasi-circular limit of the model. This prevents us from determining  $a_6^c(\nu)$  so to yield an EOB/NR phasing agreement at the level of **TEOBResumS** (see Appendix A). This problem turns out to be alleviated by using a resummed version of the 2PN-accurate *quasi-circular* reduction of  $\hat{\mathcal{F}}_r$ , starting from Eq. (5.16)

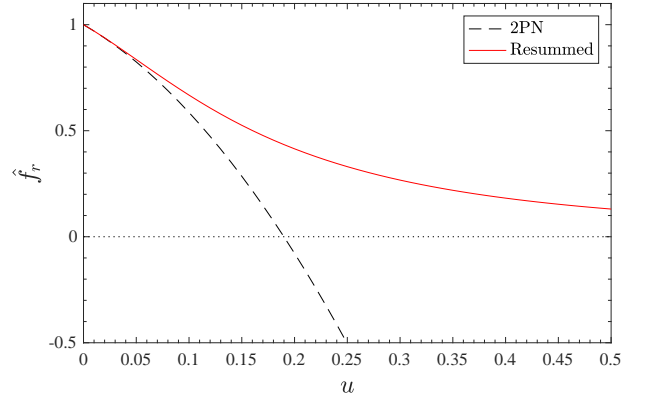


FIG. 1: Comparing the PN-expanded  $\hat{f}_r^{2\text{PN}}$ , Eq. (5), with its Padé resummed counterpart for  $q = 1$ . The resummation avoids the infinitely growing, unphysical, strong-field behavior of  $\hat{f}_r^{2\text{PN}}$ .

of Ref. [20]. The nonresummed version reads

$$\hat{\mathcal{F}}_r^{2\text{PN}} = \frac{32}{3}\nu p_r u^4 \left[ 1 - \left( \frac{1133}{280} + \frac{118}{35}\nu \right) u + \frac{1}{15120} \left( -175549 + 322623\nu + 70794\nu^2 \right) u^2 \right]. \quad (3)$$

We then proceed by replacing  $p_r = p_{r_*} \sqrt{B/A}$ , expanding at 2PN order and getting

$$\hat{\mathcal{F}}_r^{2\text{PN}} = \frac{32}{3}\nu p_{r_*} u^4 \hat{f}_r^{2\text{PN}}, \quad (4)$$

where

$$\hat{f}_r^{2\text{PN}} = 1 - \left( \frac{573}{280} + \frac{118}{35}\nu \right) u + \left( -\frac{33919}{2160} + \frac{6493}{560}\nu + \frac{1311}{280}\nu^2 \right) u^2. \quad (5)$$

The PN-expanded  $\hat{f}_r^{2\text{PN}}$  function becomes negative before, and up to, merger. This means that its effect progressively becomes unphysical (see Fig. 1). To overcome this difficulty,  $\hat{f}_r^{2\text{PN}}$  is resummed using a  $P_2^0$  Padé approximant<sup>2</sup>, not differently from what is usually done for the gyro-gravitomagnetic functions in the spin-sector of the **TEOBResumS** model [19]. In practice, our Eq. (4) is replaced by

$$\hat{\mathcal{F}}_r = \frac{32}{3}\nu p_{r_*} u^4 P_2^0 \left[ \hat{f}_r^{2\text{PN}}(u) \right], \quad (6)$$

that is then taken as default radial force in Eq. (2).

<sup>1</sup> Evidently this is also an approximation, since for uniformity the same approach should be applied also to the subdominant modes. Since, as we will see, this approximation already delivers good results, we postpone such refinement to future work.

<sup>2</sup> The natural  $P(1,1)$  approximant is unusable as it develops a spurious pole.

## B. Waveform

To include the effect brought by the generic dynamics in the waveform we essentially follow the approach of Ref. [1], that is replacing the quasi-circular Newtonian prefactor of each multipole with its generic counterpart. We report here more technical details with respect to what briefly sketched in Ref. [1]. Let us first recall the basic notation and conventions. The strain waveform is decomposed in multipoles  $h_{\ell m}$  as

$$h_+ - ih_\times = D_L^{-1} \sum_{\ell m} h_{\ell m -2} Y_{\ell m}, \quad (7)$$

where  $D_L$  is the luminosity distance and  $_{-2}Y_{\ell m}$  are the  $s = -2$  spin-weighted spherical harmonics. Following our usual practice, we will perform EOB/NR comparisons using the Regge-Wheeler-Zerilli normalized variable  $\Psi_{\ell m} = h_{\ell m} / \sqrt{(\ell+2)(\ell+1)\ell(\ell-1)}$ . Within the EOB formalism, each multipole is factorized as [21]

$$h_{\ell m} = h_{\ell m}^{(N,\epsilon)} \hat{h}_{\ell m} \hat{h}_{\ell m}^{\text{NQC}}, \quad (8)$$

where  $h_{\ell m}^{(N,\epsilon)}$  is the Newtonian (leading-order) prefactor,  $\epsilon$  the parity of  $\ell+m$ ,  $\hat{h}_{\ell m}$  is the relativistic correction that includes higher PN terms in resummed form and  $\hat{h}_{\ell m}^{\text{NQC}}$  is the NR-informed next-to-quasi-circular factor. To go beyond the quasi-circular behavior, the usual quasi-circular Newtonian prefactor  $h_{\ell m}^{(N,\epsilon)}$  is here replaced by the general expression obtained computing the time-derivatives of the Newtonian mass and current multipoles. We have  $h_{\ell m}^{(N,0)} \propto e^{im\varphi} I_{\ell m}^{(\ell)}$  and  $h_{\ell m}^{(N,1)} \propto e^{im\varphi} S_{\ell m}^{(\ell)}$ , where the superscript  $(\ell)$  indicates the  $\ell$ -th time-derivative.  $I_{\ell m} \equiv r^\ell e^{-im\varphi}$  and  $S_{\ell m} \equiv r^{\ell+1} \Omega e^{-im\varphi}$  are the Newtonian mass and current multipoles, where  $\Omega \equiv \dot{\varphi}$  is the orbital frequency. In practice, there are additional choices that can be made, multipole by multipole, and that are better explained with explicit examples. Let us focus first on the  $\ell = m = 2$  mode. The Newtonian prefactor is written as

$$h_{22}^{(N,0)} = -8\sqrt{\frac{\pi}{5}} \nu (r_\omega \Omega)^2 \left(1 + \mathcal{S}(t) \hat{h}_{22}^{\text{nc}}\right) e^{-2i\varphi}, \quad (9)$$

where  $\mathcal{S}(t)$  is a certain sigmoid function to be discussed below and the noncircular factor  $\hat{h}_{22}^{\text{nc}}$  reads

$$\hat{h}_{22}^{\text{nc}} = -\frac{1}{2} \left( \frac{\dot{r}^2}{(r\Omega)^2} + \frac{\ddot{r}}{r\Omega^2} \right) + i \left( \frac{2\dot{r}}{r\Omega} + \frac{\dot{\Omega}}{2\Omega^2} \right), \quad (10)$$

with an amplitude and a phase correction. Note that we factored out the leading order term  $(r\Omega)^2$ , where the modified EOB radius  $r_\omega$  is replacing  $r$  only in the quasi-circular prefactor of Eq. (9), so to be consistent with the standard EOB prescription for quasi-circular configurations [22, 23]. The scope of the sigmoid function

$$\mathcal{S}(t) = \frac{1}{1 + e^{\alpha(t-t_0)}}, \quad (11)$$

is to progressively switch off  $\hat{h}_{22}^{\text{nc}}$  around a given time  $t_0$ , sufficiently close to merger, as the system circularizes during late inspiral and plunge. The main reason for doing so is that  $\hat{h}_{22}^{\text{nc}}$  looks unable to correctly match the quasi-circular behavior of NR simulations in the late inspiral to plunge phase, because of the continuous growth of  $(\dot{r}, \dot{\Omega})$ . Pragmatically<sup>3</sup>, we decided to smoothly switch off  $h_{22}^{\text{nc}}$ , so to recover the usual robustness properties of the simpler quasi-circular EOB waveform. In the meanwhile, as already pointed out in Ref. [1], the next-to-quasi-circular (NQC) waveform factor  $\hat{h}_{22}^{\text{NQC}}$  is similarly switched on close to merger, to suitably modify the waveform with the NR-informed NQC parameters and provide the usual good EOB/NR match for quasi-circular binaries. For what concerns this paper, the parameters  $(\alpha, t_0)$  are chosen somehow arbitrarily:  $\alpha = 0.02$  and  $t_0 \equiv t_{\Omega^{\text{orb}}_{\text{peak}}} - 100$ , where  $t_{\Omega^{\text{orb}}_{\text{peak}}}$  is the peak time of the *pure orbital* frequency, i.e. the orbital frequency with the spin-orbit contribution subtracted [19]. For what concerns the subdominant multipoles<sup>4</sup>, up to  $\ell = m = 5$ , we adopt the following expression for each Newtonian prefactor

$$h_{\ell m}^{(N,\epsilon)} = c_{\ell m}(\nu) \left( (r_\omega \Omega)^\ell + \mathcal{S}(t) h_{\ell m}^{\text{nc}} \right) e^{-im\varphi}, \quad (12)$$

where  $c_{\ell m}(\nu)$  schematically indicate the well known Newtonian numerical coefficients, analogous<sup>5</sup> of the  $-8\sqrt{\pi/5}\nu$  in Eq. (9), and  $h_{\ell m}^{\text{nc}}$  indicates the remaining, leading order, noncircular corrections, notably not divided by  $(r\Omega)^\ell$  as in Eq. (9). We found that this non-factorized expression is generally more robust and accurate than the factorized one in all corners of the parameter space. By contrast, they are substantially equivalent for the  $(2,2)$  mode. Finally, to achieve a good compromise between accuracy and robustness, we had to slightly modify the prescription for  $\hat{h}_{\ell m}^{\text{NQC}}$  presented in Ref. [16], to which we refer the reader for all precise technical details concerning the determination procedure of NQC corrections. Just to clarify the logic, we only recall here that the NQC correction factor reads

$$\hat{h}_{\ell m}^{\text{NQC}} = (1 + a_1^{\ell m} n_1 + a_2^{\ell m} n_2) e^{i(b_1^{\ell m} n_3^{\ell m} + b_2^{\ell m} n_4^{\ell m})}, \quad (13)$$

where  $n_i^{\ell m}$ , with  $i = 1 \dots 4$ , are functions depending on the radial momentum, while  $(a_i^{\ell m}, b_i^{\ell m})$ , with  $i = 1, 2$ , are NR-informed numerical coefficients<sup>6</sup>. For the  $\ell = m = 2$  mode, the  $n_i^{22}$  functions are given by Eqs. (3.32)-(3.35)

<sup>3</sup> One could have chosen different, though Newtonian-like consistent, forms for  $\hat{h}_{22}^{\text{nc}}$ , e.g. by replacing  $\dot{r}$  with  $p_{r_*}$  as it is done to obtain the analytical structure of  $\hat{h}_{\ell m}^{\text{NQC}}$  [16]. We did not explore this option since the application of the straight Newtonian expression already looked sufficiently accurate for our purposes.

<sup>4</sup> We recall that we do not taken into account  $m = 0$  modes.

<sup>5</sup> See e.g. Eqs. (3.21)-(3.30) of [16] for their explicit values.

<sup>6</sup> The procedure implemented for their determination is detailed in Sec. IIID of Ref. [16].

TABLE I: Informing the nonspinning sector of the model. From left to right the columns report: the dataset number, the SXS identification number; the mass ratio  $q$ ; the symmetric mass ratio  $\nu$ ; the first guess value of  $a_6^c$  and the fitted value from Eq. (14).

#	SXS	$q$	$\nu$	$a_6^c$	$a_6^c(\nu)$
1	SXS:BBH:0180	1	0.25	280	281.62
2	SXS:BBH:0007	1.5	0.24	200	198.63
3	SXS:BBH:0184	2	0.2	110	102.75
4	SXS:BBH:0259	2.5	0.204	36	48.61
5	SXS:BBH:0294	3.5	0.173	14	8.56
6	SXS:BBH:0295	4.5	0.149	0	-1.18
7	SXS:BBH:0056	5	0.139	-1	-2.78
8	SXS:BBH:0063	8	0.0988	-5	-3.61
9	SXS:BBH:0303	10	0.0826	-5.1	-3.1

of [16]. For higher modes, we implement the following modifications with respect to the prescriptions of Ref. [16], Eqs. (3.38)-(3.45) in order to improve their robustness all over the parameter space. In particular, for  $\ell = m = 3$  and  $\ell = m = 4$ , we have that  $n_4^{\ell m} = n_3^{\ell m} \Omega^{2/3}$  when the spins are negative, while  $n_4^{\ell m} = n_3^{\ell m} (r\Omega)^2$  for *positive* spins. In addition, we also use  $n_2^{32} = n_1^{32} \Omega^{2/3}$ ;  $n_2^{43} = n_1^{43} \Omega^{2/3}$ ,  $n_2^{42} = n_2^{42} \Omega^{2/3}$  and  $n_4^{42} = n_3^{42} (r\Omega)^2$  instead of Eq.(3.42)-(3.45) of [16]. This is meaningful seen the effective nature of the NQC correction factor: its choice has to compensate/improve the bare, purely analytical, part of the waveform whose (resummed) PN accuracy depends on the multipole [17].

### C. Determining the $a_6^c$ and $c_3$ functions.

To determine new expressions for  $(a_6^c, c_3)$  we follow our usual procedure, discussed extensively e.g. in Ref. [16–18]. The approach simply relies on monitoring the time-evolution of the EOB/NR phase difference between waveforms aligned in the early inspiral while varying  $(a_6^c, c_3)$ . We follow a two-step procedure, by first informing the nonspinning sector of the model and then the spinning one. To start with, we consider 9 nonspinning simulations (see Table I), and determine for each one the value of  $a_6^c$  that makes the EOB/NR phase difference at NR merger of the order of (or smaller than) the nominal NR uncertainty, which is estimated taking the phase difference between the highest and second highest numerical resolution (see Table V of Ref. [24] for this calculation). Following the standard procedure within the **TEOBResumS** waveform paradigm [16–18, 24, 25], these few points are determined, by hand and without any automatized procedure, by simply inspecting the phase differences on time-domain phasing plots and checking that the EOB/NR phase difference at merger is within the

TABLE II: Informing the spinning sector of the model. From left to right the columns report: the dataset number, the SXS identification number; the mass ratio and the individual dimensionless spins  $(q, \chi_1, \chi_2)$ ; the first-guess values of  $c_3$  used to inform the global interpolating fit given in Eq. (16), and the corresponding  $c_3^{\text{fit}}$  values.

#	ID	$(q, \chi_1, \chi_2)$	$c_3^{\text{first guess}}$	$c_3^{\text{fit}}$
1	SXS:BBH:0156	(1, -0.95, -0.95)	89	88.822
2	SXS:BBH:0159	(1, -0.90, -0.90)	86.5	86.538
3	SXS:BBH:0154	(1, -0.80, -0.80)	81	81.508
4	SXS:BBH:0215	(1, -0.60, -0.60)	70.5	70.144
5	SXS:BBH:0150	(1, +0.20, +0.20)	26.5	26.677
6	SXS:BBH:0228	(1, +0.60, +0.60)	16.0	15.765
7	SXS:BBH:0230	(1, +0.80, +0.80)	13.0	12.920
8	SXS:BBH:0153	(1, +0.85, +0.85)	12.0	12.278
9	SXS:BBH:0160	(1, +0.90, +0.90)	11.5	11.595
10	SXS:BBH:0157	(1, +0.95, +0.95)	11.0	10.827
11	SXS:BBH:0004	(1, -0.50, 0)	54.5	46.723
12	SXS:BBH:0231	(1, +0.90, 0)	24.0	23.008
13	SXS:BBH:0232	(1, +0.90, +0.50)	15.8	16.082
14	SXS:BBH:0005	(1, +0.50, 0)	34.3	27.136
15	SXS:BBH:0016	(1.5, -0.50, 0)	57.0	49.654
16	SXS:BBH:0016	(1.5, +0.95, +0.95)	13.0	11.720
17	SXS:BBH:0255	(2, +0.60, 0)	29.0	23.147
18	SXS:BBH:0256	(2, +0.60, +0.60)	20.8	17.37
19	SXS:BBH:0257	(2, +0.85, +0.85)	14.7	14.56
20	SXS:BBH:0036	(3, -0.50, 0)	60.0	53.095
21	SXS:BBH:0267	(3, -0.50, -0.50)	69.5	60.37
22	SXS:BBH:0174	(3, +0.50, 0)	30.0	24.210
23	SXS:BBH:0291	(3, +0.60, +0.60)	23.4	19.635
24	SXS:BBH:0293	(3, +0.85, +0.85)	16.2	17.759
25	SXS:BBH:1434	(4.368, +0.80, +0.80)	20.3	20.715
26	SXS:BBH:0060	(5, -0.50, 0)	62.0	55.385
27	SXS:BBH:0110	(5, +0.50, 0)	31.0	24.488
28	SXS:BBH:1375	(8, -0.90, 0)	64.0	71.91
29	SXS:BBH:0064	(8, -0.50, 0)	57.0	55.385
30	SXS:BBH:0065	(8, +0.50, 0)	28.5	24.306
31	BAM	(8, +0.80, 0)	24.5	22.605
32	BAM	(8, +0.85, +0.85)	14.0	22.199

corresponding NR uncertainty<sup>7</sup>. Due to the robustness of the theoretical framework, these points are easily fitted to get

$$a_6^c(\nu) = \left( -0.50395 - 4.8547\nu + 52.96\nu^2 \right) e^{20.7013\nu}. \quad (14)$$

<sup>7</sup> This is estimated taking the difference between the highest and second highest resolution available for each dataset

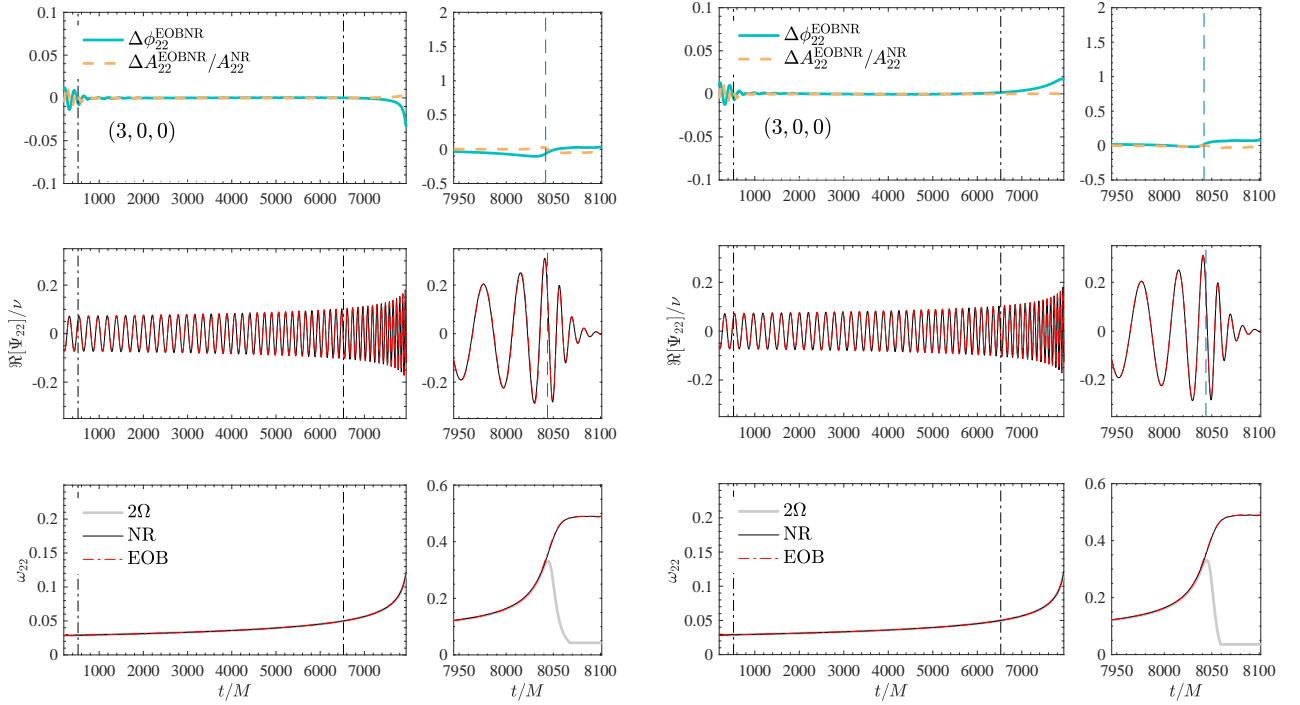


FIG. 2: EOB/NR comparison with the 27-orbits long  $q = 3$ , quasi-circular, nonspinning dataset SXS:BBH:1221. Left panel: phasing comparison with the **TEOBResumSGeneral** model discussed in this paper, endowed with the generic waveform and radiation reaction. Right panel: phasing comparison with the quasi-circular **TEOBResumS** model. Top panel: (relative) amplitude and phase difference (in radians). Middle panel: real part of the waveform. Bottom panel: gravitational frequencies. For convenience, also twice the EOB orbital frequency  $2\Omega$  is shown on the plot. The dash-dotted vertical lines indicate the alignment frequency region, while the dashed one the merger time.

Although this result is reliable and accurate for our purposes, we note that the functional form is *not* quasi-linear as for **TEOBResumS** case [17]. The exponential is needed to accommodate the rather large values of  $a_r^c$  found as  $\nu \rightarrow 0.25$  and it is related to the fact that  $\tilde{\mathcal{F}}_r \neq 0$ . To get a quantitative idea of the EOB/NR agreement yielded by our new analytical choices, Fig. 2 reports two EOB/NR phasing comparisons corresponding to the  $q = 3$  case (EOB/NR comparison is discussed extensively in Ref.[23]). The left panel shows the phasing obtained with the general, **TEOBResumSGeneral** EOB model that is discussed here, while the right panel is obtained using **TEOBResumS**. The top panel shows the (relative) amplitude and phase differences, the middle panel the real part of the EOB (red) and NR (black) waveforms and the bottom panel the gravitational frequencies. In the bottom panel is also shown twice the EOB orbital frequency  $2\Omega$ . The dash-dotted vertical lines indicate the alignment frequency region, that adopts the standard procedure discussed in Ref. [23]. The NR dataset we chose to compare with is SXS:BBH:1221. This is a 27-orbits long simulations that was *not* used at all to inform any of the two models. The phasing plots illustrate that the eccentric EOB model accumulates a secular dephasing with respect to the NR waveform that is of the order of 0.1 rad at merger (vertical dashed line), slightly larger than, but compatible with the **TEOBResumS** one. As

usual, the figure of merit of the quality of the EOB waveform is given by the EOB/NR unfaithfulness weighted by the Advanced LIGO noise. Considering two waveforms  $(h_1, h_2)$ , the unfaithfulness is a function of the total mass  $M$  of the binary and is defined as

$$\bar{F}(M) \equiv 1 - F = 1 - \max_{t_0, \phi_0} \frac{\langle h_1, h_2 \rangle}{\|h_1\| \|h_2\|}, \quad (15)$$

where  $(t_0, \phi_0)$  are the initial time and phase. We used  $\|h\| \equiv \sqrt{\langle h, h \rangle}$ , and the inner product between two waveforms is defined as  $\langle h_1, h_2 \rangle \equiv 4\Re \int_{f_{\min}^{\text{NR}}(M)}^{\infty} \tilde{h}_1(f) \tilde{h}_2^*(f) / S_n(f) df$ , where  $\tilde{h}(f)$  denotes the Fourier transform of  $h(t)$ ,  $S_n(f)$  is the zero-detuned, high-power noise spectral density of Advanced LIGO [26] and  $f_{\min}^{\text{NR}}(M) = \hat{f}_{\min}^{\text{NR}}/M$  is the initial frequency of the NR waveform at highest resolution, i.e. the frequency measured after the junk-radiation initial transient. Waveforms are tapered in the time-domain so as to reduce high-frequency oscillations in the corresponding Fourier transforms. The EOB/NR unfaithfulness is addressed as  $\bar{F}_{\text{EOB/NR}}$ . We will also consider  $\bar{F}_{\text{NR/NR}}$ , as Eq. (15) computed between the highest and second highest resolution waveforms available, that we will quote as an indication of the NR uncertainty (see also Sec.III B of Ref.[17]). When computing this  $\bar{F}_{\text{EOB/NR}}$  for SXS:BBH:1221, we obtain  $\bar{F}_{\text{EOB/NR}}^{\text{max}} \equiv \max_M [\bar{F}_{\text{EOB/NR}}(M)] = 0.14\%$ , that,

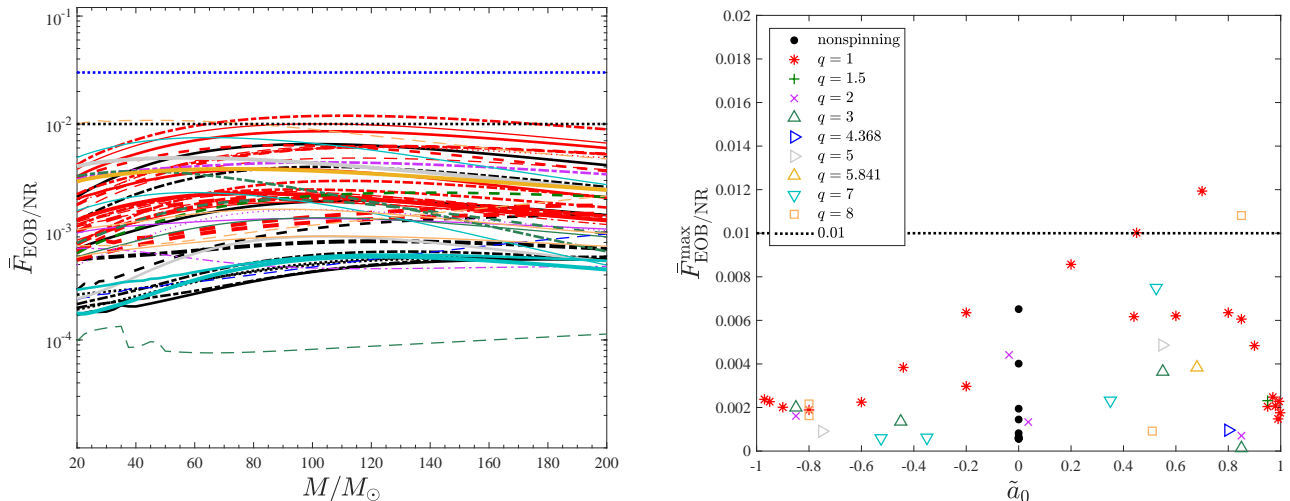


FIG. 3: Quasi-circular configurations. Left panel: EOB/NR unfaithfulness for the  $\ell = m = 2$  mode. A subset of this data is used to inform the  $(a_6^c, c_3)$  functions as explained in the text. The phasing performance is acceptably at most of the order of 0.01, though it is less good than the standard quasi-circular **TEOBResumS** model [2]. The maximal values  $\bar{F}_{\text{EOB/NR}}^{\text{max}} \equiv \max_M[\bar{F}_{\text{EOB/NR}}(M)]$  are shown in the right panel (see also Tables V-VI). Note the two outliers slightly above the 0.01 threshold.

though a satisfactory value, is one order of magnitude larger than the value  $\bar{F}_{\text{EOB/NR}}^{\text{max}} = 0.0157\%$  obtained with **TEOBResumS** (see Table XIX of [17]) corresponding to the time-domain phasing comparison in the right panel of Fig. 2. This is the typical case for the nonspinning NR datasets we have considered (see Table V). For example, for SXS:BBH:0180 we obtain  $\bar{F}_{\text{EOB/NR}}^{\text{max}} = 0.65\%$  to be contrasted with  $\bar{F}_{\text{EOB/NR}}^{\text{max}} = 0.0873\%$  obtained with **TEOBResumS** (see Table XVIII of Ref. [17]). The main technical motivation behind this difference is the fact that the eccentric model uses  $\hat{\mathcal{F}}_r \neq 0$ , while **TEOBResumS** was imposing by construction  $\hat{\mathcal{F}}_r = 0$ . Even though, as pointed out in Appendix A, the quasi-circular expression of  $\hat{\mathcal{F}}_r$  that we are using has a relatively mild behavior towards merger that allows for a reasonably accurate NR-tuning of  $a_6^c(\nu)$ , the global model turns out to perform worse than when imposing  $\hat{\mathcal{F}}_r = 0$  by construction<sup>8</sup>. One has to remember, however, that all these statements are relative to an EOB conservative dynamics that employs a Padé (1, 5) resummation of the  $A$  potential, with the (resummed)  $B$  (or  $D$ ) function taken at 3PN accuracy. Given the effective character of the resummation procedures used (and in particular of the NR-tuning of the parameters) a priori one cannot exclude that either (i) a different resummation of the potentials or (ii) different PN truncations may eventually result in an increased flexibility of the model that could yield a closer EOB/NR agreement. These issues deserve detail and systematic investigations that will hopefully be carried out in future

work.

The new functional form of  $a_6^c(\nu)$  given by Eq. (14) calls for a similarly new determination of the effective spin-orbit parameter  $c_3$ . We do so using a set of NR data that is slightly different from the one used in Ref. [17] so to improve the robustness of the model in certain corners of the parameter space. The NR datasets used are listed in Table II. Following Ref. [17], for each dataset we report the value of  $c_3^{\text{first guess}}$  obtained by comparing EOB and NR phasing so that the accumulated phase difference is of the order of the NR uncertainty (and/or so that consistency between NR and EOB frequencies around merger is achieved as much as possible). Similarly to the case of  $a_6^c$ , the robustness of the model allows us to efficiently do this by hand without any automatized procedure. The  $c_3^{\text{first guess}}$  values of Table II are fitted with a global function of the spin variables  $\tilde{a}_i \equiv S_i/(m_i M)$  with  $i = 1, 2$  of the form

$$c_3(\tilde{a}_1, \tilde{a}_2, \nu) = p_0 \frac{1 + n_1 \tilde{a}_0 + n_2 \tilde{a}_0^2 + n_3 \tilde{a}_0^3 + n_4 \tilde{a}_0^4}{1 + d_1 \tilde{a}_0} + p_1 \tilde{a}_0 \nu \sqrt{1 - 4\nu} + p_2 (\tilde{a}_1 - \tilde{a}_2) \nu^2 + p_3 \tilde{a}_0 \nu^2 \sqrt{1 - 4\nu}, \quad (16)$$

where  $\tilde{a}_0 \equiv \tilde{a}_1 + \tilde{a}_2$  and the functional form is the same of previous works<sup>9</sup>. This term helps in improving the fit flexibility as the mass ratio increases. The fitting coeffi-

<sup>8</sup> This can be considered as a sort of gauge condition for the circularized dynamic [20].

<sup>9</sup> Note that this function is not symmetric for exchange of  $1 \leftrightarrow 2$ . This can create an ambiguity for  $q = 1$ , so that the value of  $c_3$  for  $(1, 0.6, 0.4)$  is in fact different from the one for  $(1, 0.4, 0.6)$ . In fact, our convention and implementations are such that for  $q = 1$ ,  $\chi_1$  is *always* the largest spin.

cients read

$$p_0 = 35.482253, \quad (17)$$

$$n_1 = -1.730483, \quad (18)$$

$$n_2 = 1.144438, \quad (19)$$

$$n_3 = 0.098420, \quad (20)$$

$$n_4 = -0.329288, \quad (21)$$

$$d_1 = -0.345207, \quad (22)$$

$$p_1 = 244.505, \quad (23)$$

$$p_2 = 148.184, \quad (24)$$

$$p_3 = -1085.35. \quad (25)$$

We finally test the performance of Eq. (16) by computing  $\bar{F}_{\text{EOB/NR}}$  over a set of 43 spinning configurations that is only partially overlapping with the one used to determine it. The configurations are chosen so to efficiently cover the parameter space, in particular including its difficult corners (i.e. large mass ratio and large spins). This choice is motivated by the fact that previous work showed that most of the 595, spin-aligned, SXS simulations available are in fact redundant among themselves and do not bring additional information from the EOB/NR testing point of view [17]. The behavior of  $\bar{F}_{\text{EOB/NR}}(M)$  is shown in Fig. 3, that also includes 10 nonspinning datasets. All values of  $\bar{F}_{\text{EOB/NR}}^{\text{max}}$  are listed in Tables V-VI and are also plotted in the right panel of Fig. 3 versus  $\tilde{a}_0$ , so to have an immediate perception of the model performance all over the parameter space. The outliers, slightly above 1%, occur for  $0.4 \lesssim \tilde{a}_0 \lesssim 0.8$  for  $q = 1$  as well as for large values of  $\tilde{a}_0$  when  $q = 8$ . Although it is probably further improvable, we believe that this level of EOB/NR agreement is sufficient for our current purposes.

#### D. Higher modes

The performance of the higher modes is similar to the one of **TEOBResumS**, although we have seen that the robustness of the waveform completion through the NQC correction factor tends to decrease as the mass ratio or the individual spins are increased. This problem was already pointed out in Ref. [16], and it is known to appear when the peak of the considered subdominant multipole is significantly delayed with respect to the (2, 2) one. This is typically the case for modes with  $m \neq \ell$  when spins are large and anti-aligned with the angular momentum. Therefore, the modes with  $\ell = m$  are, on average, the most robust through merger and ringdown all over the parameter space. However, when spins are large and anti-aligned with the angular momentum, the dynamics is such to prevent the NQC factor to work correctly already for modes like (3, 3) and (4, 4). This is for example the case of (3, -0.85, -0.85), while for (3, -0.50, -0.50) the application of the NQC factor yields a perfectly sound multipolar waveform. The other, most relevant, subdominant modes (2, 1), (3, 2), (4, 3), (4, 2)

are certainly always reliable through merger and ringdown when the spin magnitudes are small (i.e. up to approximately  $|\chi_i| \simeq 0.5$ ) and  $q \lesssim 6$ , but it might not be the case for larger, negative, spins. To highlight a few cases where everything falls correctly into place, Fig. 4 refers to EOB/NR comparisons of amplitudes and frequencies for configuration  $(q, \chi_1, \chi_2) = (6, 0, 0)$ . For completeness of information, the figure also displays the EOB quantities without the NQC factor (orange online) and without the ringdown attachment (light-blue online). The vertical dashed line indicates the NR merger location, i.e. the peak of the (2, 2) NR waveform. The frequency panel also displays, as a gray dotted line, the time evolution of the orbital frequency. Note that the behavior of both the orange and light-blue lines after the merger point is unphysical, though we prefer to keep it as additional information. As usual, the behavior of the bare EOB waveform, both amplitude and frequency, is already highly consistent with the NR waveform, without need of additional tuning, up to about  $50M$  (or less) before merger. The differences in the ringdown part, especially large for (3, 2), (4, 3) and (4, 2) come from the absence of mode-mixing [27–29] in the ringdown on the EOB side.

As a spinning example, Fig. 5 illustrates the same multipoles as Fig. 4 but for  $(q, \chi_1, \chi_2) = (3, +0.30, +0.30)$ . Qualitatively, the most relevant visual difference between Fig. 4 and Fig. 5 on the EOB side concerns the amplitude of modes (3, 2) and (4, 3) that is larger than the corresponding NR one. There are other configurations where the NQC-corrected EOB waveform performs similarly or worse, possibly affecting also the frequency that becomes very large and unphysical before the ringdown attachment. This effect is more and more marked (until it eventually gets unphysical) the more the peak of the considered NR multipole is displaced on the right with respect to the (2, 2) one. A precise quantification of the limits of reliability and robustness of the current EOB multipolar model is beyond the scope of this work. Qualitatively, however, the considerations already driven in Ref. [16] with special focus on the (2, 1) mode for large, anti-aligned spins still hold here, with no new conceptual findings. A quick analysis that we performed for several mass ratios and spin values points, again, to the fact that the Achilles' heel of the EOB models based on the **TEOBResumS** paradigm resides in the NQC determination procedure. We think that the procedure of informing the multipolar NQC parameters with NR information extracted *after* the multipole peak as it is done now should be revised, since it necessarily relies on a part of the EOB dynamics (i.e. beyond the location of the usual merger) that, at the moment, is not fully under control for certain configurations [18].



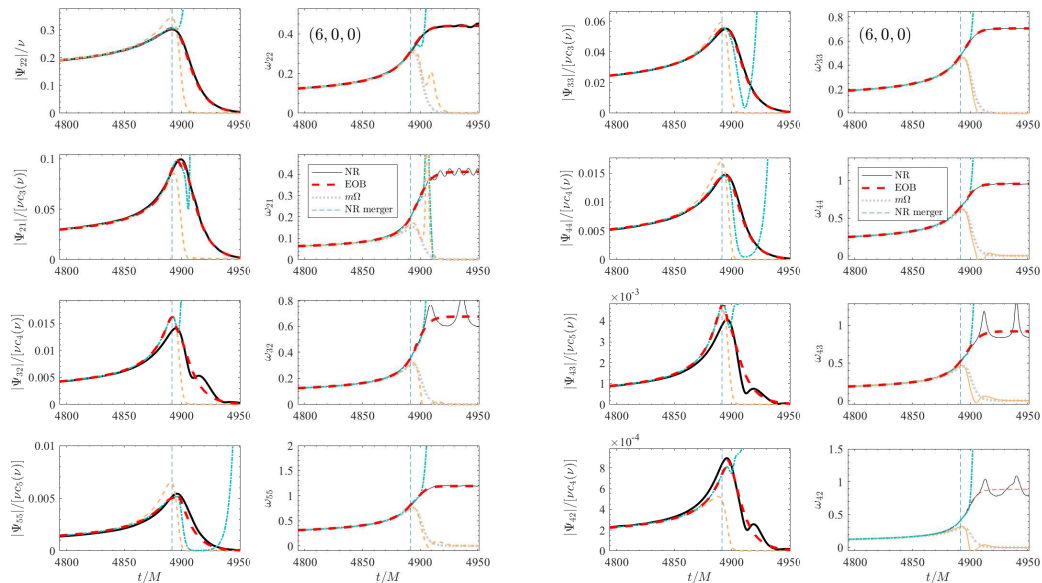


FIG. 4: EOB/NR multipolar comparison of amplitude and frequency for  $(q, \chi_1, \chi_2) = (6, 0, 0)$ , referring to SXS:BBH:0166 dataset. The grey, dotted, line reports  $m\Omega$ , where  $\Omega$  is the EOB orbital frequency. The picture also displays the EOB analytical waveform (orange online) and the NQC completed one (light-blue online). The vertical line indicates the NR merger time, i.e. the peak of the  $(2, 2)$  amplitude.

### III. ECCENTRIC CONFIGURATIONS

#### A. Numerical Relativity waveforms

##### 1. NR eccentricity

Here we consider all the 28 eccentric SXS datasets currently public, the nonspinning ones being published in Ref. [30]. As done in Ref. [1], it is instructive to evaluate the initial eccentricity of each NR simulation using some eccentricity estimator, so to obtain a simple intuition about the waveform properties<sup>10</sup>. Inspired by previous work, Ref. [31] introduced an eccentricity estimator

$$e_\Omega(t) = \frac{\sqrt{\Omega_p^{\text{NR}} - \Omega_a^{\text{NR}}}}{\sqrt{\Omega_p} + \sqrt{\Omega_a}}, \quad (26)$$

that uses the NR *orbital* frequencies  $\Omega_a^{\text{NR}}$  and  $\Omega_p^{\text{NR}}$  at apastron and periastron extracted from the puncture trajectories. Reference [31] made this choice because the gravitational wave frequency computed from the NR simulations (obtained using the Einstein Toolkit [32] and not the SpEC code) considered there was too noisy to be used in Eq. (26). By contrast, here (as it was previously done

in [1]) we find that it is actually possible to apply such eccentricity estimator directly on the GW frequency  $\omega_{22}^{\text{NR}}$  of the SXS simulations. To do so efficiently and more reliably, however, we need to remove some high frequency noise present at the very beginning of the simulations just after the junk radiation, especially in those with larger eccentricities. The noise removal is simply done using a Savitzky-Golay filter implemented in the commercial software **Matlab**. Such straightforward procedure allows us to cleanly identify the maxima (periastron,  $\omega_p^{\text{NR}}$ ) and the minima (apastron,  $\omega_a^{\text{NR}}$ ) of  $\omega_{22}^{\text{NR}}$ . These quantities are then fitted versus time using a rational function of the form

$$\omega_{a,p}^{\text{NR}} = c_{a,p} \frac{1 + n_{a,p}t}{1 + d_{a,p}t}. \quad (27)$$

Our estimate of the NR eccentricity,  $e_\omega^{\text{NR}}$ , is then obtained from Eq. (26) by replacing  $\Omega_{a,p}^{\text{NR}}$  with  $\omega_{a,p}^{\text{NR}}$ . This procedure is applied to all NR simulations of Table III and Fig. 6 shows the time evolution of the corresponding  $e_\omega^{\text{NR}}$ . The first point of each curve corresponds to the frequency of the first apastron,  $\omega_a^{\text{NR}}$ . The third column of Table III precisely lists these values  $e_{\omega_a}^{\text{NR}}$ , while the fourth column displays the corresponding frequency  $\omega_a^{\text{NR}}$ .

##### 2. NR uncertainty

To complement what we did already in Ref. [1], and to better evaluate the performance of the EOB model in the

<sup>10</sup> Note however that this eccentricity is not going to play any role within the EOB model.



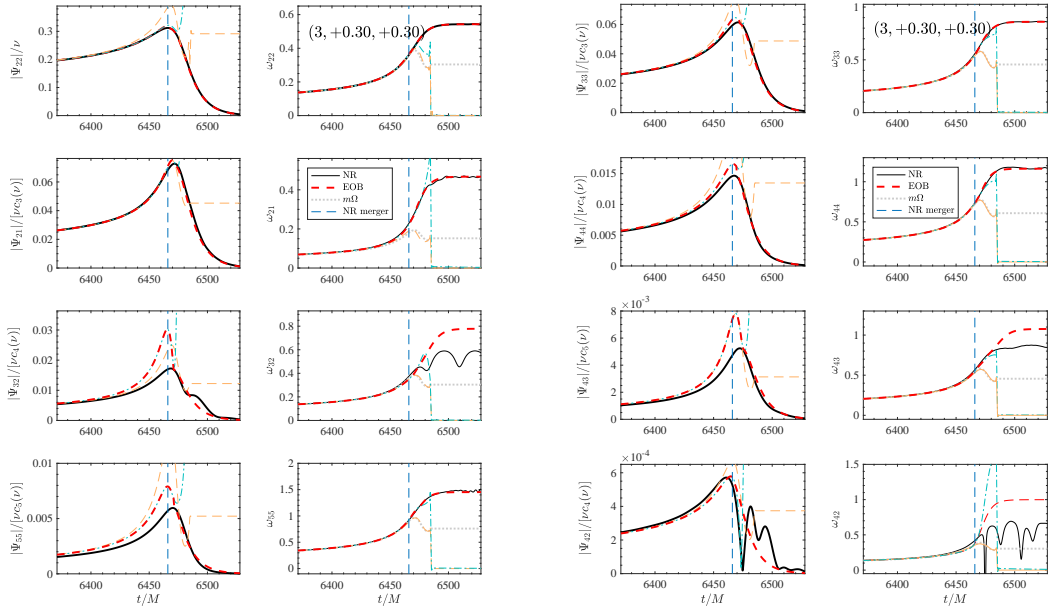


FIG. 5: EOB/NR multipolar comparison of amplitude and frequency for  $(q, \chi_1, \chi_2) = (3, +0.30, +0.30)$ , referring to SXS:BBH:2155 dataset. The grey, dotted, line reports  $m\Omega$ , where  $\Omega$  is the EOB orbital frequency. The picture also displays the EOB inspiral analytical waveform (orange online) and the NQC completed one (light-blue online). The vertical line indicates the NR merger time, i.e. the peak of the (2, 2) amplitude. Note the EOB amplitude of some subdominant modes is overestimated towards merger.

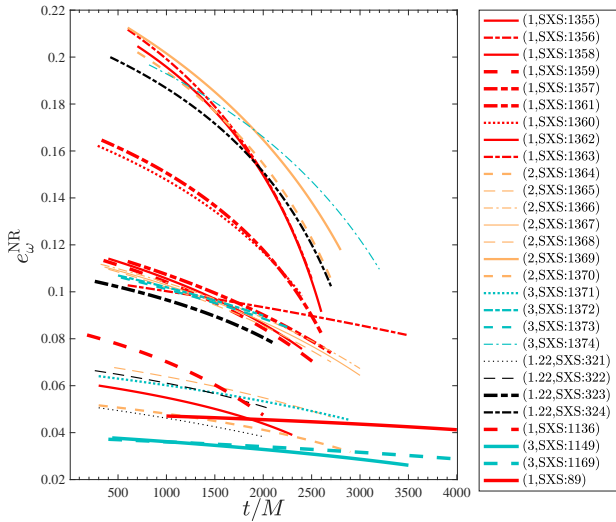


FIG. 6: Time evolution of the NR eccentricity estimated using Eq. 26 applied to the GW frequency at apastron and periastron, Eq. (27). The initial point of each curve corresponds to the values at the first apastron,  $e_{\omega_a}^{\text{NR}}$ , listed in Table III.

next section, we provide here an explicit error estimate on the eccentric NR simulations that we are considering, repeating and extending the analysis of Ref. [30], that was limited to nonspinning configurations. All SXS datasets we use are listed in Table III. We use the highest and second highest resolutions available in the SXS catalog to give two, complementary, error estimates. On

the one hand, we compute the time-domain phase difference  $\delta\phi^{\text{NR}}$  for the  $\ell = m = 2$  waveform mode between the highest and second highest resolution and retain its value at the high-resolution merger point  $\delta\phi_{\text{mrg}}^{\text{NR}}$ . This value appears in the third column of Table III. A few comments are in order. First, for all nonspinning dataset, this quantity is *at most*  $\sim 1$  rad, often less. Although this number is a useful indicator of a, probably overestimated, accumulated NR uncertainty, in itself it might hide details that require the inspection of the full time evolution of  $\delta\phi^{\text{NR}}(t)$ . In fact one easily realizes that not all NR simulations seem to have the same quality. For some dataset,  $\delta\phi^{\text{NR}}(t)$  is smooth and clean, with a quality comparable to the one of standard quasi-circular simulations. In other cases,  $\delta\phi^{\text{NR}}(t)$  is very noisy, with large oscillations within the  $\pm 0.1$  band. This is clearly illustrated in Fig. 7 for the two situations mentioned above: the highly eccentric configuration SXS:BBH:1370, that presents large amplitude oscillations, and a mildly eccentric one, SXS:BBH:1355, where  $\delta\phi^{\text{NR}}(t)$  looks much better behaved. These details can influence the quality of EOB/NR phasing comparisons, as we will mention below. The  $\delta\phi_{\text{mrg}}^{\text{NR}}$  for spinning datasets, last eight rows of Table III, are typically rather large, and do not really give a useful, stringent, measure of the error bar. We note that  $\delta\phi^{\text{NR}}$  for SXS:BBH:324 shows a similar behavior to the one of SXS:BBH:1370, with large oscillations during the inspiral, so that the value  $\delta\phi_{\text{mrg}}^{\text{NR}} = -0.04$  may not faithfully reflect the actual quality of the data.

As a complementary accuracy estimate, we also evaluate the unfaithfulness  $\bar{F}_{\text{NR/NR}} \equiv 1 - F_{\text{NR/NR}}$ , using

TABLE III: SXS simulations with eccentricity analyzed in this work. From left to right: the ID of the simulation; the mass ratio  $q \equiv m_1/m_2 \geq 1$  and the individual dimensionless spins  $(\chi_1, \chi_2)$ ; the time-domain NR phasing uncertainty at merger  $\delta\phi_{\text{mrg}}^{\text{NR}}$ ; the estimated NR eccentricity at first apastron  $e_a^{\text{NR}}$ ; the NR frequency of first apastron  $\omega_a^{\text{NR}}$ ; the initial EOB eccentricity  $e_a^{\text{EOB}}$  and apastron frequency  $\omega_a^{\text{EOB}}$  used to start the EOB evolution; the maximal NR unfaithfulness uncertainty,  $\bar{F}_{\text{NR/NR}}^{\text{max}}$  and the maximal EOB/NR unfaithfulness,  $\bar{F}_{\text{EOB/NR}}^{\text{max}}$ .

#	id	$(q, \chi_1, \chi_2)$	$\delta\phi_{\text{mrg}}^{\text{NR}} [\text{rad}]$	$e_a^{\text{NR}}$	$\omega_a^{\text{NR}}$	$e_a^{\text{EOB}}$	$\omega_a^{\text{EOB}}$	$\bar{F}_{\text{NR/NR}}^{\text{max}} [\%]$	$\bar{F}_{\text{EOB/NR}}^{\text{max}} [\%]$
1	SXS:BBH:1355	(1, 0, 0)	+0.92	0.0620	0.03278728	0.0890	0.02805750	0.012	0.96
2	SXS:BBH:1356	(1, 0, 0)	+0.95	0.1000	0.02482006	0.15038	0.019077	0.0077	0.91
3	SXS:BBH:1358	(1, 0, 0)	+0.25	0.1023	0.03108936	0.18078	0.021238	0.016	1.07
4	SXS:BBH:1359	(1, 0, 0)	+0.25	0.1125	0.03708305	0.18240	0.02139	0.0024	0.88
5	SXS:BBH:1357	(1, 0, 0)	-0.44	0.1096	0.03990101	0.19201	0.01960	0.028	0.88
6	SXS:BBH:1361	(1, 0, 0)	+0.39	0.1634	0.03269520	0.23557	0.0210	0.057	1.090
7	SXS:BBH:1360	(1, 0, 0)	-0.22	0.1604	0.03138220	0.2429	0.01959	0.0094	1.04
8	SXS:BBH:1362	(1, 0, 0)	-0.09	0.1999	0.05624375	0.3019	0.01914	0.0098	0.84
9	SXS:BBH:1363	(1, 0, 0)	+0.58	0.2048	0.05778104	0.30479	0.01908	0.07	1.04
10	SXS:BBH:1364	(2, 0, 0)	-0.91	0.0518	0.03265995	0.08464	0.025231	0.049	0.42
11	SXS:BBH:1365	(2, 0, 0)	-0.90	0.0650	0.03305974	0.11015	0.023987	0.027	0.50
12	SXS:BBH:1366	(2, 0, 0)	$-6 \times 10^{-4}$	0.1109	0.03089493	0.1496	0.02580	0.017	0.84
13	SXS:BBH:1367	(2, 0, 0)	+0.60	0.1102	0.02975257	0.15065	0.026025	0.0076	0.50
14	SXS:BBH:1368	(2, 0, 0)	-0.71	0.1043	0.02930360	0.14951	0.02527	0.026	0.41
15	SXS:BBH:1369	(2, 0, 0)	-0.06	0.2053	0.04263738	0.3134	0.01735	0.011	0.58
16	SXS:BBH:1370	(2, 0, 0)	+0.12	0.1854	0.02422231	0.31445	0.016915	0.07	0.88
17	SXS:BBH:1371	(3, 0, 0)	+0.92	0.0628	0.03263026	0.0912	0.029058	0.12	0.39
18	SXS:BBH:1372	(3, 0, 0)	+0.01	0.1035	0.03273944	0.14915	0.026070	0.06	0.32
19	SXS:BBH:1373	(3, 0, 0)	-0.41	0.1028	0.03666911	0.15035	0.0253	0.0034	0.23
20	SXS:BBH:1374	(3, 0, 0)	+0.98	0.1956	0.02702594	0.31388	0.016946	0.067	0.23
21	SXS:BBH:89	(1, -0.50, 0)	...	0.0469	0.02516870	0.07201	0.01779	...	0.60
22	SXS:BBH:1136	(1, -0.75, -0.75)	-1.90	0.0777	0.04288969	0.12105	0.02728	0.074	0.41
23	SXS:BBH:321	(1.22, +0.33, -0.44)	+1.47	0.0527	0.03239001	0.07621	0.02694	0.015	0.71
24	SXS:BBH:322	(1.22, +0.33, -0.44)	-2.02	0.0658	0.03396319	0.0984	0.026895	0.016	0.93
25	SXS:BBH:323	(1.22, +0.33, -0.44)	-1.41	0.1033	0.03498377	0.1438	0.02584	0.019	0.77
26	SXS:BBH:324	(1.22, +0.33, -0.44)	-0.04	0.2018	0.02464165	0.29414	0.01894	0.098	1.06
27	SXS:BBH:1149	(3, +0.70, +0.60)	+3.00	0.0371	0.03535964	0.0623	0.02664	0.025	0.33
28	SXS:BBH:1169	(3, -0.70, -0.60)	+3.01	0.0364	0.02759632	0.04895	0.024285	0.033	0.096

Eq. (15) above, between the two highest NR resolutions using the `zero_det_highP` [33] Advanced-LIGO power spectral density. Figure 8 displays  $\bar{F}_{\text{NR/NR}}$  for all SXS datasets available except for SXS:BBH:0089, that is given in the catalog with a single resolution. The corresponding values of  $\bar{F}_{\text{NR/NR}}^{\text{max}} \equiv \max(\bar{F}_{\text{NR/NR}})$  are listed in the sixth column of Table III. The picture highlights that there are three simulations that have larger uncertainties during the inspiral, that corresponds to the small  $M$  region. As we will see below, especially by inspecting higher modes of SXS:BBH:324, these are datasets whose quality should possibly be improved to better exploit them in the future for EOB/NR comparison purposes.

## B. EOB waveforms: choosing initial conditions

To provide meaningful EOB/NR comparison, the EOB dynamics should be started in such a way that the eccentricity induced modulations in the EOB waveform are consistent with the corresponding ones present in the NR simulations. We follow previous work (including the generalization of ID setup of Ref. [34] to spinning binaries) so to setup initial data using a nominal EOB eccentricity parameter  $e^{\text{EOB}}$ . This is not strictly neces-

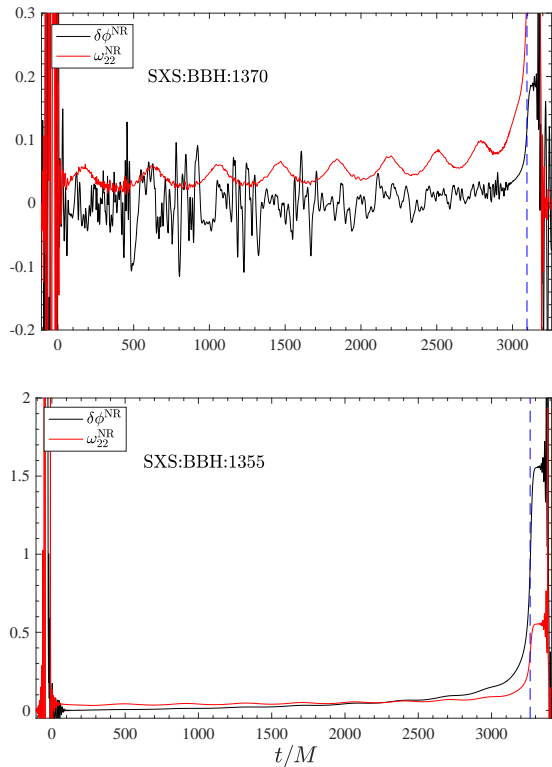


FIG. 7: Time domain estimate of the nominal NR phase uncertainty  $\delta\phi^{\text{NR}}$  obtained taking the phase difference between the two highest resolutions available. We also report the NR frequency of the  $\ell = m = 2$  mode  $\omega_{22}^{\text{NR}}$ . The vertical dashed line corresponds to the merger of the dataset with the highest resolution. For SXS:BBH:1370 the large oscillations present during the inspiral suggest that the quality of the waveform is lower than for the SXS:BBH:1355 case. Note however the clean evolution of  $\delta\phi^{\text{NR}}$  towards merger and the corresponding rather small value of  $\delta\phi_{\text{mrg}}^{\text{NR}}$ .

sary<sup>11</sup> (especially because, differently from Ref. [34] we do not express the EOB dynamics using it), but it is just intuitively convenient. So, as it was done in Ref. [1], the eccentricity-related modulation of the EOB dynamics and waveform are controlled via the initial gravitational wave quadrupole frequency at apastron,  $\omega_a^{\text{EOB}}$  and initial EOB eccentricity at the same frequency  $e_{\omega_a}^{\text{EOB}}$ . From these parameters, one then determines, via quasi-Newtonian formulas following Ref. [34], an initial semilatus rectum and from this an initial separation and angular momentum. The radial momentum is always set to zero since the EOB dynamics is started, by construction, at apastron. The procedure for correctly finding the EOB values that allow for a best match between waveforms is slightly tricky and cannot be fully automatized.

<sup>11</sup> The EOB dynamics is ruled by initial energy and angular momentum. So, one could simply setup the system at apastron in the same way as it is done for hyperbolic configurations [2].

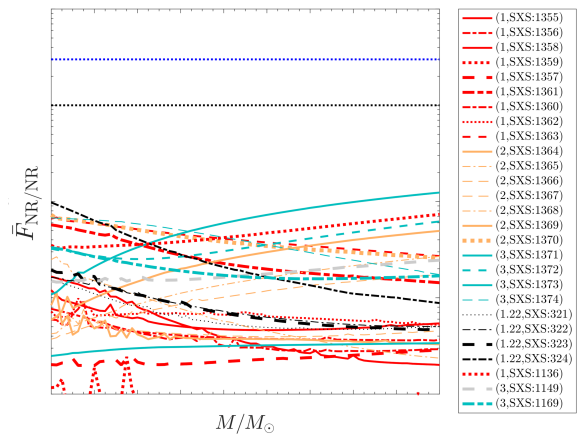


FIG. 8: Estimate of the NR uncertainty  $\bar{F}_{\text{NR}/\text{NR}}$  computing  $\bar{F}$  from Eq. (15) between the highest and second highest resolution level for each NR simulation. The horizontal lines mark the 0.03 and 0.01 values. Datasets SXS:BBH:324, SXS:BBH:1361 and SXS:BBH:1369 have the largest uncertainties during the inspiral.

Let us discuss it in some detail. For an initial guess of  $(\omega_a^{\text{EOB}}, e_{\omega_a}^{\text{EOB}})$ , motivated by the values of the corresponding NR quantities, the EOB and NR waveforms are aligned in the time-domain with our usual procedure [35] during the inspiral. Then, we compute the fractional EOB/NR frequency difference  $\Delta\omega_{22}^{\text{EOBNR}} \equiv \omega_{22}^{\text{EOB}} - \omega_{22}^{\text{NR}}$  and inspect it versus time. We then vary, recursively, first  $\omega_a^{\text{EOB}}$  and then  $e_{\omega_a}^{\text{EOB}}$ , until we make  $\Delta\omega_{22}^{\text{EOBNR}}$  as small as possible ( $\simeq 10^{-2}$  or less) and as nonoscillatory as possible over the longest inspiral time interval. In practice, we monitor  $\Delta\omega_{22}^{\text{EOBNR}}$  and allow it to eventually grow only during the plunge up to merger and ring-down. For doing so efficiently one has to remember that increasing  $e^{\text{EOB}}$  translates into a stronger GW emission at the periastron and thus a shorter waveform, i.e. the inspiral gets accelerated. If  $e_{\omega_a}^{\text{EOB}}$  is decreased, it is true the opposite and the inspiral gets longer. The procedure is very sensitive to minimal variations of the parameters  $(\omega_a^{\text{EOB}}, e_{\omega_a}^{\text{EOB}})$ . Typically, one has to vary  $\omega_a^{\text{EOB}}$  in steps of order  $10^{-4}$  and  $e^{\text{EOB}}$  in steps of order  $10^{-5}$  to achieve an acceptable phasing agreement. Figure 9 displays two examples of the outcome of this procedure, for SXS:BBH:1356 (smaller eccentricity,  $e_{\omega}^{\text{NR}} \sim 0.1$ ) and SXS:BBH:1374 (larger eccentricity,  $e_{\omega}^{\text{NR}} \sim 0.2$ ). For each simulations we show, superposed, the EOB and NR frequencies, together with  $\Delta\omega_{22}^{\text{EOBNR}}$ . The figure corresponds to the values of  $(\omega_a^{\text{EOB}}, e_{\omega_a}^{\text{EOB}})$  in Table III. For SXS:BBH:1356  $\Delta\omega_{22}^{\text{EOBNR}}$  is found to oscillate around zero within  $\pm 5 \times 10^{-3}$  for most of the time, but it grows during plunge up to merger time. Interestingly, despite being marred by high-frequency noise,  $\Delta\omega_{22}^{\text{EOBNR}}$  essentially averages zero also for SXS:BBH:1374, thus confirming the quality of our parameter choice. The picture remains essentially the same for all simulations we considered, except for SXS:BBH:1370. For this dataset, it

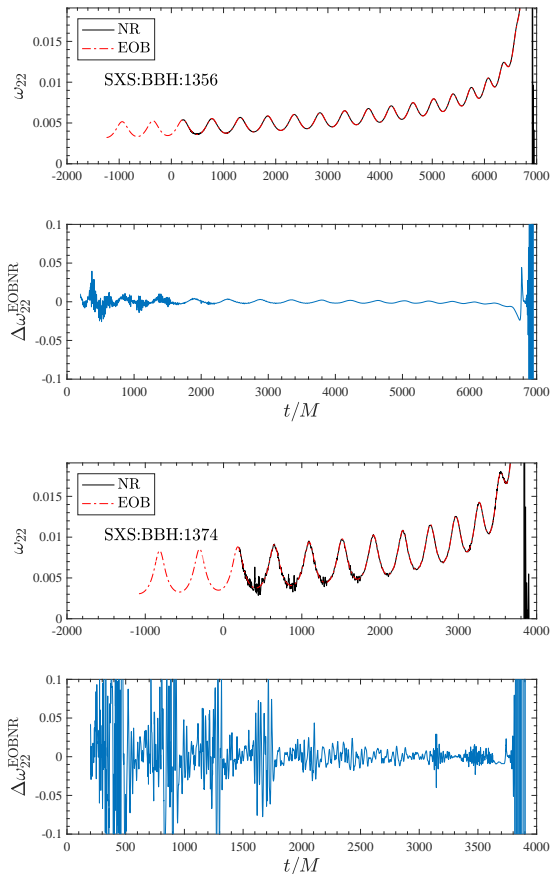


FIG. 9: EOB/NR gravitational wave frequency,  $\omega_{22}^{\text{EOB/NR}}$ , agreement for two illustrative SXS datasets with smaller eccentricity (top panels) and larger eccentricity (bottom panels) obtained suitably varying the initial parameters ( $\omega_a^{\text{EOB}}, e^{\text{EOB}}$ ). The parameters are chosen so that the fractional phase difference  $\Delta\omega_{22}^{\text{EOBNR}} \equiv \omega_{22}^{\text{EOB}} - \omega_{22}^{\text{NR}}$  averages zero for the longest time interval (that excludes merger and ringdown) and with small amplitude, secular, oscillations.

doesn't seem possible to optimize ( $\omega_a^{\text{EOB}}, e^{\text{EOB}}$ ) to flatten the secular oscillation in  $\Delta\omega_{22}^{\text{EOBNR}}$  during the early inspiral. As mentioned above, this is probably due to the slightly lower quality of the SXS:BBH:1370 simulation with respect to the others. Modulo this case, we found that the procedure is robust and reliable all over the dataset at our disposal, although it is sensitive to small variations and a careful fine tuning is needed. Our current best choices of ( $\omega_a^{\text{EOB}}, e^{\text{EOB}}$ ) are listed in Table III.

### C. EOB/NR phasing and unfaithfulness: the quadrupole mode

We start the discussion of the EOB/NR phasing comparisons focusing on Fig. 10. The figure shows together EOB/NR phasings for SXS:BBH:1359, a mildly eccentric dataset with  $e_a^{\text{NR}} = 0.11$  and mass ratio  $q = 1$ , as well

as for SXS:BBH:1374 that has larger initial eccentricity,  $e_a^{\text{NR}} \sim 0.2$  and  $q = 3$ . For each dataset, the figure shows: the EOB/NR phase difference  $\Delta\phi_{22}^{\text{EOBNR}}$  (top panel); the EOB and NR real part of the waveform (middle panel); the EOB and NR frequencies (bottom panel). The figure highlights that our choice of ( $e^{\text{EOB}}, \omega_a^{\text{EOB}}$ ) is such to also yield a rather flat phase difference during the inspiral, with just small amplitude residual oscillations, that are always confined between  $\pm 0.05$ . These differences are of the same order (actually a bit larger) than the corresponding NR error uncertainties obtained by taking the phase difference between the two highest resolutions available. The behavior of the phase difference illustrated in Fig. 10 remains approximately the same for all other configurations. As mentioned above, an exception is represented by the, apparently less accurate, SXS:BBH:1370 dataset, where it does not seem possible to reduce  $\Delta\phi_{22}^{\text{EOBNR}}$  below  $\pm 0.2$  rad. Similarly, despite varying and fine tuning methodically the initial parameters, it doesn't seem possible to obtain phase differences that look perfectly flat on the  $[-0.1, +0.1]$  rad scale, likewise the quasi-circular case, see Fig. 2. This does not look surprising in view of the fact that noncircular effects in both waveform and radiation reaction are incorporated only through the leading order Newtonian factors. Additional improvements are expected to occur by including, probably in some resummed form, up to 3PN noncircular terms, see e.g. [36, 37]

The quality of the model is finally assessed by computing the EOB/NR unfaithfulness  $\bar{F}_{\text{EOB/NR}}$ . As discussed in Ref. [30], the clean computation of the Fourier transform is trickier than the quasi-circular case and a more aggressive tapering is needed to avoid effects due to Gibbs phenomenon. Figure 11 shows the result of  $\bar{F}_{\text{EOB/NR}}$  computation using, as in the circular case, the Advanced LIGO sensitivity curve. The improvement with respect to Fig. 4 of [1] is dramatic, with  $\bar{F}_{\text{EOB/NR}}^{\text{max}}$  at most of order 1%, visually rather similar to the performance of the circularized case, Fig. 3. The figure is complemented by the values of  $\bar{F}_{\text{EOB/NR}}^{\text{max}}$  listed in the last column of Table III. The most interesting thing to note is that there are little differences between the low-eccentricity and high-eccentricity cases, and in all cases  $\bar{F}_{\text{EOB/NR}}^{\text{max}} \simeq 1\%$ . This suggests, somehow surprisingly, that the treatment of noncircular effects via the general Newtonian prefactor could be acceptably accurate (i.e.  $\bar{F}_{\text{EOB/NR}}^{\text{max}} \lesssim 3\%$ ) also for *larger eccentricities*. A thorough assessment of this statement would require additional SXS eccentric simulations at least as accurate as the ones currently available.

### D. Subdominant modes

Reference [1] already pointed out that it is also possible to obtain a good agreement between EOB and NR higher multipolar modes by simply replacing each circularized Newtonian factor with the corresponding noncircular

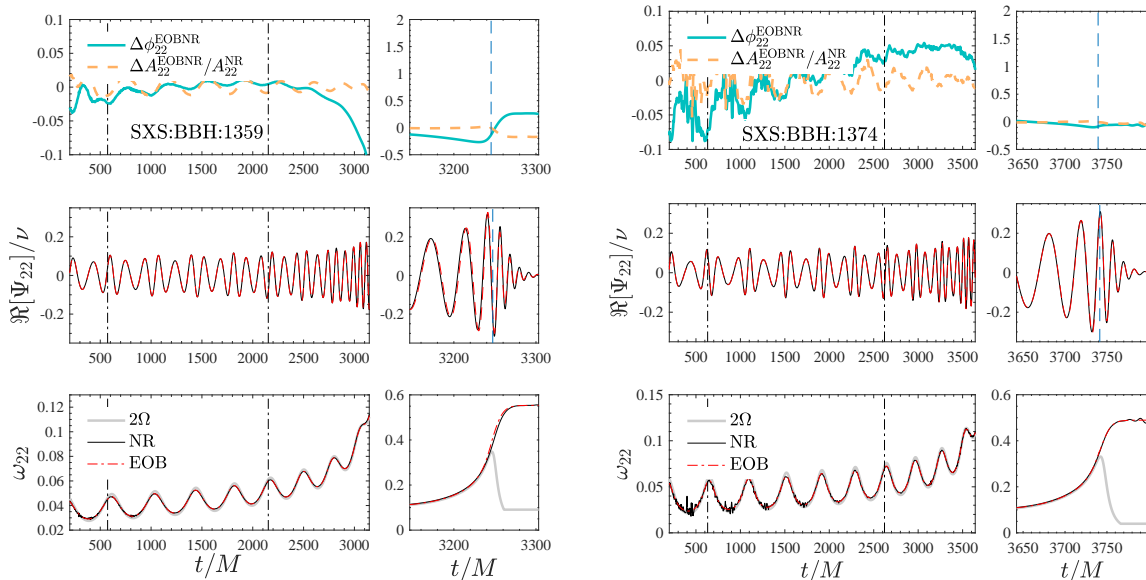


FIG. 10: EOB/NR time-domain phasing comparison for nonspinning configurations. Left panels: SXS:BBH:1359,  $q = 1$ ,  $e_{\omega_a}^{\text{NR}} \simeq 0.11$ . Right panels: SXS:BBH:1374,  $q = 3$ ,  $e_{\omega_a}^{\text{NR}} \simeq 0.2$ . The vertical dash-dotted lines indicate the alignment interval, while the dashed vertical line the merger time. With  $\Omega$  we address the EOB orbital frequency (gray online). Note the excellent EOB/NR phasing agreement during the eccentric inspiral.

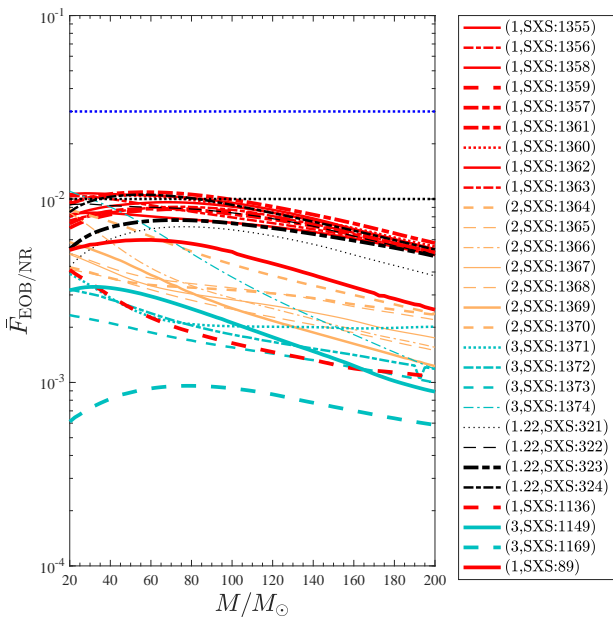


FIG. 11: EOB/NR unfaithfulness computed over the eccentric SXS simulations publicly available. The horizontal lines mark the 0.03 and 0.01 values.

counterpart. The purpose of this section is to show this explicitly for a sample of significative NR datasets. We focus on 4 specific configurations: SXS:BBH:1371 (large mass ratio, low eccentricity), Fig. 12; SXS:BBH:1374 (large mass ratio, large initial eccentricity,  $e_{\omega_a}^{\text{NR}} \simeq 0.2$ ), Fig. 13; SXS:BBH:324, a configuration with large eccentricity  $e_{\omega_a}^{\text{NR}} \simeq 0.2$ , unequal mass and unequal spins,

Fig. 14; and SXS:BBH:1136, equal-mass, small eccentricity  $e_{\omega_a}^{\text{NR}} \simeq 0.08$ , but large spins, anti-aligned with the orbital angular momentum, Fig. 15. Figures 12-14 display all meaningful multipoles, that is  $(2, 2)$ ,  $(2, 1)$ ,  $(3, 3)$ ,  $(3, 2)$ ,  $(4, 3)$ ,  $(4, 4)$  and  $(5, 5)$ , while Fig. 15 only shows  $(2, 2)$  and  $(4, 4)$ . In all figures, the vertical dashed line indicates the NR merger location. Waveforms are always aligned during the inspiral. The phase and amplitude agreement is satisfactory in all cases. In particular, it is interesting to note that the waveforms remain well in phase, including the higher modes, *also* when the eccentricity is large, i.e. for SXS:BBH:1374 and SXS:BBH:324, Figs. 13 and 14, even if in these two cases some of the NR higher modes (see e.g. the  $(5, 5)$ ) are marred by high-frequency numerical noise. This is an interesting fact that allows the EOB waveform to be used as benchmark to further improve the quality of the NR simulations. This is especially interesting for a small-amplitude mode like the  $(4, 2)$ : once the NR high-frequency noise clears up (see e.g. the bottom right panels of Figs. 13 and 14), the late-inspiral waveform is found to be well consistent with the analytical prediction. By contrast, focusing on Fig. 14, let us also note that the amplitude of the analytical  $(4, 3)$  mode gets progressively too large towards merger due to the unphysical action of the NQC correction factor that we discussed above. Similarly, differences during ringdown in modes like  $(3, 2)$ ,  $(4, 3)$  and  $(4, 2)$  are due to the absence of mode-mixing effects [27–29].



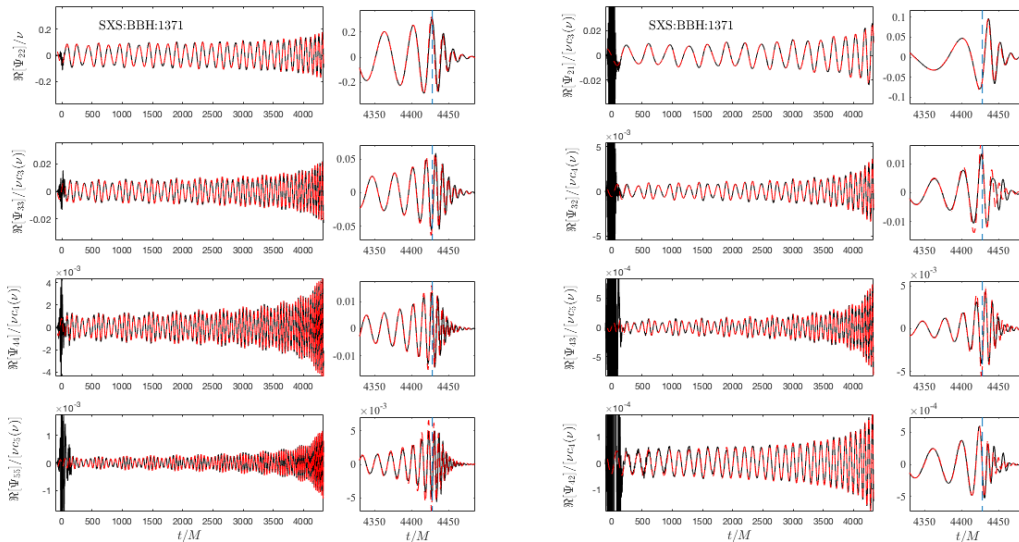


FIG. 12: EOB/NR multipolar phasing agreement for SXS:BBH:1371, with  $(3,0,0)$  and initial  $e_{\omega_a}^{\text{NR}} \simeq 0.06$ . Waves are aligned during the early inspiral. The vertical dashed line indicate the NR merger location. The EOB waveform inspiral is robust and reliable *also* for modes like  $(5,5)$  and  $(4,2)$ , where the corresponding NR data are typically plagued by high-frequency numerical noise.

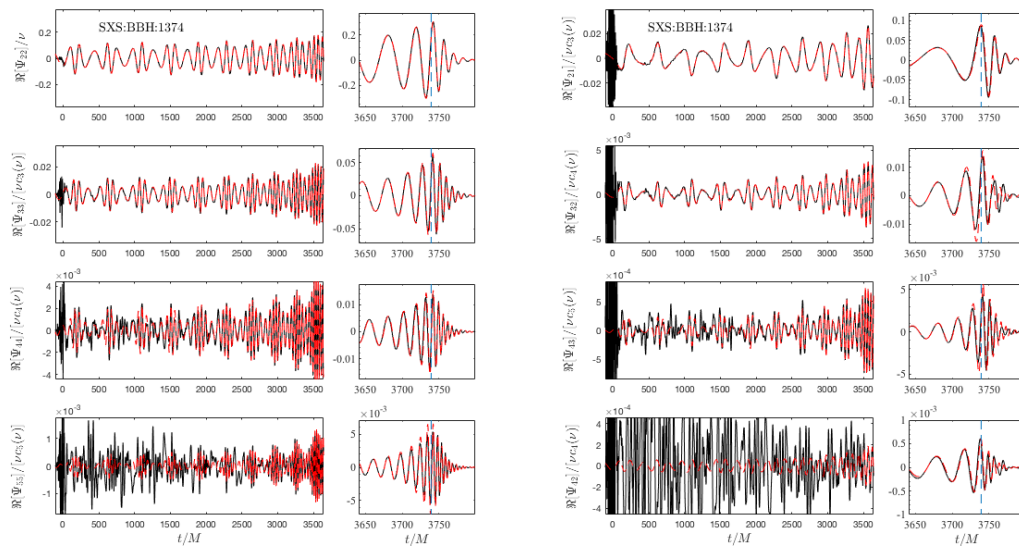


FIG. 13: EOB/NR multipolar phasing agreement for SXS:BBH:1374, with  $(3,0,0)$  and initial  $e_{\omega_a}^{\text{NR}} \simeq 0.2$ . Waves are aligned during the early inspiral. The vertical dashed lines indicate the NR merger location. The EOB/NR phasing and amplitude agreement is excellent all over the inspiral up to merger and ringdown, modulo mode-mixing effects during ringdown for  $(3,2)$ ,  $(4,3)$  and  $(4,2)$  multipoles.

#### IV. HYPERBOLIC ENCOUNTERS AND SCATTERING ANGLE

Recently, Ref. [2] showed how the EOB model can be used to compute dynamics and waveforms from hyper-

bolic encounters. See Ref. [38, 39] for a recent overview. Recently, Ref. [40] also pointed out that these events may be detectable by the present and next-generation ground-based observatories. Accurate modelization of dynamics and waveform is then needed. Both the (i)



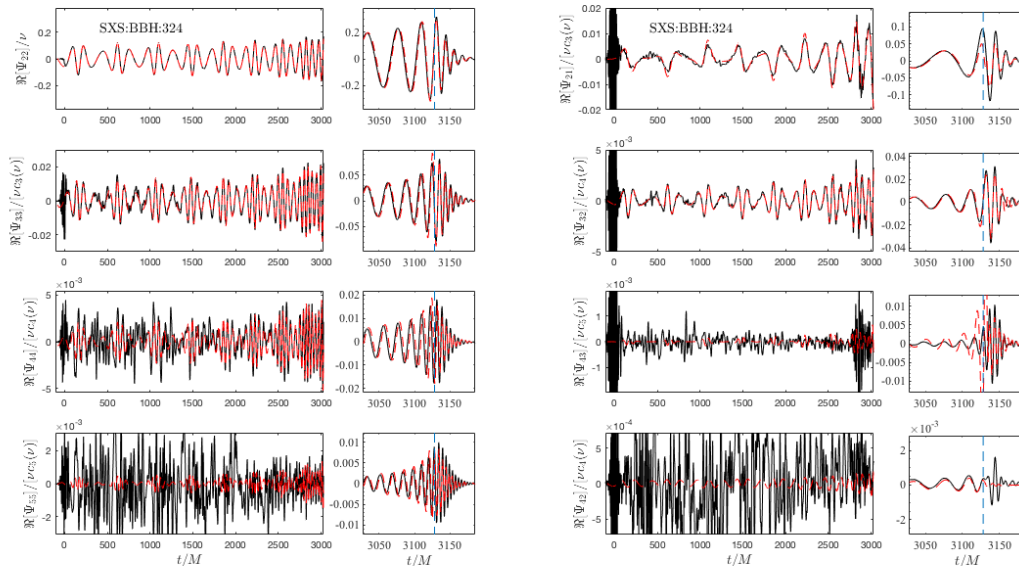


FIG. 14: Multipolar phasing agreement between EOB (red online) and NR (black online) waveform for SXS:BBH:324, with  $(1.22, +0.33, -0.44)$  and  $e_{\omega_a}^{\text{NR}} \simeq 0.2$ . This is currently the most eccentric and general spin-aligned configuration available in the SXS catalog. Waves are aligned during inspiral. The vertical dashed lines indicate the NR merger location. Note the rather large numerical noise in many of the NR subdominant multipoles, especially the  $(4, 2)$  that is completely unreliable. For mode  $(4, 3)$ , the NQC correction factor introduces well known unphysical effects in the amplitude during late inspiral.

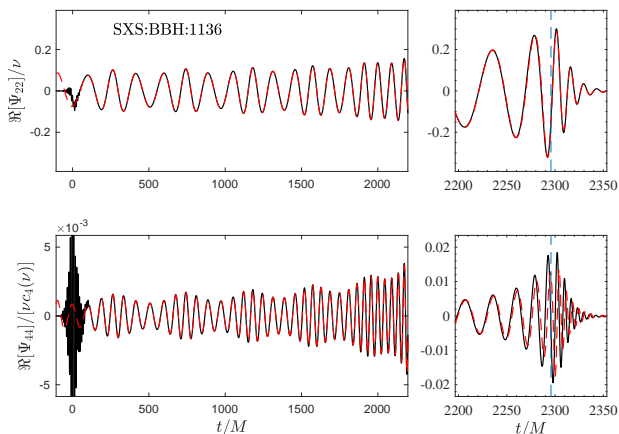


FIG. 15: EOB/NR phasing comparison for the nonzero even-parity modes for SXS:BBH:1136 dataset, with  $(1, -0.75, -0.75)$  and  $e_{\omega_a}^{\text{NR}} \simeq 0.08$ . Waveforms are aligned during the inspiral, while the vertical dashed line indicates the merger position. The corresponding  $(2, 2)$  EOB/NR phase difference oscillates between  $-0.05$  and  $0.05$  rad during the inspiral, to eventually accumulate  $-0.5$  rad at merger point.

new expressions of  $(\hat{\mathcal{F}}_\varphi, \hat{\mathcal{F}}_r)$  and (ii) the new determination of  $(a_6^c, c_3)$  will have a quantitative impact on the results of [2], although the basic phenomenology of hyperbolic encounters and dynamical captures remains the same discussed there. It is however informative to re-

peat here the EOB calculation of the scattering angle  $\chi$  for the 10 configurations simulated in NR [41] and that are discussed in Table I of [2]. The EOB outcome, together with the original NR values,  $(\chi^{\text{EOB}}, \chi^{\text{NR}})$  is listed in Table IV, that is visually complemented by Fig. 16. The Table also reports the GW energy,  $\Delta E$ , and angular momentum,  $\Delta J$ , losses for both the NR simulations and the EOB dynamics<sup>12</sup>. The figure also plots for convenience the results of Ref. [2]. The EOB/NR agreement is now rather good, with a marked improvement with respect to [2] for the first 4 configurations, that correspond to the smallest values of the EOB impact parameter  $r_{\text{min}}$ . Notably, configuration #1, that was directly plunging in Ref. [2], is now found to have the correct qualitative scattering behavior, with a quantitative EOB/NR fractional difference that is of 12%. This fact is a reliable cross check of the consistency and robustness of our procedure to obtain  $a_6^c(\nu)$ : although the function was determined using quasi-circular configurations, its impact looks to be essentially correct *also* for scattering configuration. For what concerns the comparisons between the energy and angular momentum losses, the agreement between  $(\Delta E^{\text{NR}}, \Delta E^{\text{EOB}})$  is pretty sta-

<sup>12</sup> Let us specify that while the NR losses are computed from the waveform, the EOB losses are computed subtracting the initial and final energy and angular momentum, i.e. effectively accounting for the action of the radiation reaction on the dynamics.

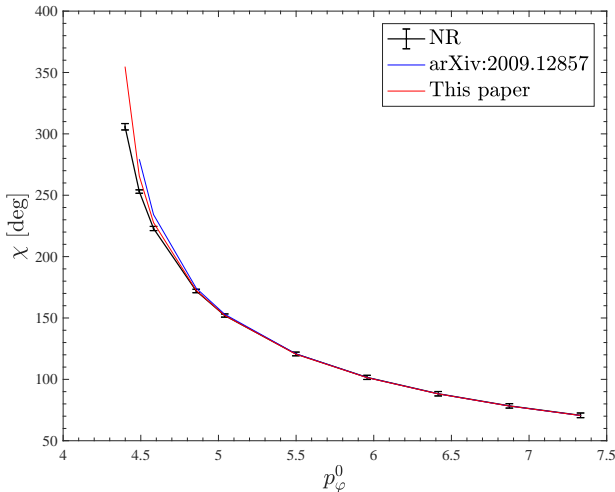


FIG. 16: Visual EOB/NR comparison of the scattering angles of Table IV. To appreciate the improvement reached here we also list the EOB points computed in Table I of [2].

ble, with absolute fractional differences of few percents, ranging from 8.9% for #10 to 6.75% for #1. By contrast, the  $(\Delta J^{\text{NR}}, \Delta J^{\text{EOB}})$  difference is rather large,  $\sim 44\%$  for #10, to get progressively better and better as the impact parameter diminishes, up to only  $\sim 0.6\%$  for #1. This looks like a promising starting point for future investigations, that aim at improving both the conservative dynamics, e.g. including higher order terms in the EOB potentials (see e.g. Ref. [2]), and the radiation reaction beyond the quasi-circular limit.

## V. CONCLUSIONS

We have presented an improvement of the EOB model of Ref. [1] for generic, spin-aligned, coalescing black hole binaries, **TEOBResumSGeneral**. The main, new, technical aspect of the model concerns the fact that its quasi-circular limit is now correctly informed by NR waveform data. This allows us to have a single, NR-faithful, waveform model for spin-aligned binaries that can deal with any kind of configuration, from quasi-circular to eccentric and hyperbolic. Our main findings are as follows:

- (i) In the quasi-circular limit, the model is compared with a significative fraction of the SXS waveform catalog (including mass ratios up to  $q = 10$  and the largest spins available) by providing the usual EOB/NR unfaithfulness  $\bar{F}_{\text{EOB/NR}}$  computation using the Advanced LIGO power spectral density. We find that  $\bar{F}_{\text{EOB/NR}} \simeq 1\%$  except for a single outlier,  $(8, +0.85, +0.85)$  (obtained with the BAM code) that still is  $< 2\%$ . Although the performance is not as good as the one of the standard quasi-circular **TEOBResumS** model [17], it is below the usual 3% threshold used as figure of merit. We postpone to future studies a precise investigation of how this

performance translates on parameter estimation. We would also like to stress that the availability of two different, though rather similar, EOB models based on the same analytical structure, and with comparable EOB/NR performances, will allow one to put on a very solid ground any statement about *analytic systematics*. In particular, it will be interesting to understand to which extent a minimal degradation of the  $\bar{F}_{\text{EOB/NR}}$  function, determined by well defined modifications in the model (e.g., the presence or absence of  $\hat{\mathcal{F}}_r$ ) impacts the inferred parameters.

- (ii) For eccentric binaries, in stable configurations, we have obtained a notable improvement with respect to the results of Ref. [1], with  $\bar{F}_{\text{EOB/NR}}^{\text{max}} \lesssim 1\%$  for all available eccentric SXS configurations. We stress that eccentric NR data are used *only* to test the model and not to inform it. On the one hand, this indicates that our eccentric model is mature enough for being used in parameter estimation on all GW BBH sources already detected. On the other hand, the rather easy, though successful, approach that we followed already calls for improvements, either to accurately deal with even larger eccentricities or to see whether  $\bar{F}_{\text{EOB/NR}}^{\text{max}}$  can be lowered further, possibly to reach the same level of the standard quasi-circular model,  $\bar{F}_{\text{EOB/NR}}^{\text{max}} \simeq 10^{-3}$ . Concerning larger initial eccentricities, it will be useful to have additional, public, SXS simulations of the same quality (or possibly higher) of the current ones. NR simulations with higher initial eccentricities, up to  $\simeq 0.4$ , do exist [31], but this data are private<sup>13</sup> and not available for our purposes.
- (iii) We have shown that higher modes in presence of eccentricity are also largely reliable, and often more accurate than the corresponding NR ones, especially during the inspiral.
- (iv) For hyperbolic scattering, the model provides values of the scattering angle (and of the GW energy losses) that are highly consistent with few NR computations currently available, especially for small values of the impact parameter, improving quantitatively the results of Ref. [2].
- (v) The waveform model discussed here is publicly available as stand-alone C-implementation, that is released via a **bitbucket** git repository [42], within the eccentric branch. See also Appendix C for additional technical details. Although a precise assessment of the performance of the model for parameter estimation purposes is beyond the scope

<sup>13</sup> Note however that this data were obtained using the Einstein Toolkit [32] and how their quality compares to the one of the SXS ones should be carefully studied.

TABLE IV: Comparison between EOB and NR scattering angle. From left to right the columns report: the ordering number; the EOB impact parameter  $r_{\min}$ ; the NR and EOB radiated energies,  $(\Delta E^{\text{NR}}/M, \Delta E^{\text{EOB}}/M)$ ; the NR and EOB radiated angular momentum,  $(\Delta J^{\text{NR}}/M^2, \Delta J^{\text{EOB}}/M^2)$ ; the NR and EOB scattering angles  $(\chi^{\text{NR}}, \chi^{\text{EOB}})$  and their fractional difference  $\hat{\Delta}\chi^{\text{NREOB}} \equiv |\chi^{\text{NR}} - \chi^{\text{EOB}}|/\chi^{\text{NR}}$ . The EOB/NR agreement is improved with to Ref. [2], see Table I there and Fig. 16.

#	$r_{\min}$	$\Delta E^{\text{NR}}/M$	$\Delta E^{\text{EOB}}/M$	$\Delta J^{\text{NR}}/M^2$	$\Delta J^{\text{EOB}}/M^2$	$\chi^{\text{NR}}$ [deg]	$\chi^{\text{EOB}}$ [deg]	$\hat{\Delta}\chi^{\text{NREOB}}$ [%]
1	3.43	0.01946(17)	0.021348	0.17007(89)	0.176789	305.8(2.6)	354.782050	16.0177
2	3.79	0.01407(10)	0.013453	0.1380(14)	0.123928	253.0(1.4)	265.604256	4.9819
3	4.09	0.010734(75)	0.009610	0.1164(14)	0.096685	222.9(1.7)	227.722810	2.1637
4	4.89	0.005644(38)	0.004623	0.076920(80)	0.057576	172.0(1.4)	172.446982	0.2599
5	5.37	0.003995(27)	0.003183	0.06163(53)	0.044608	152.0(1.3)	152.028075	0.0181
6	6.52	0.001980(13)	0.001529	0.04022(53)	0.027405	120.7(1.5)	120.481058	0.1814
7	7.61	0.0011337(90)	0.000870	0.029533(53)	0.019026	101.6(1.7)	101.389990	0.2067
8	8.68	0.007108(77)	0.000549	0.02325(47)	0.014190	88.3(1.8)	88.150825	0.1689
9	9.74	0.0004753(75)	0.000372	0.01914(76)	0.011103	78.4(1.8)	78.268033	0.1683
10	10.79	0.0003338(77)	0.000266	0.0162(11)	0.008993	70.7(1.9)	70.536902	0.2307

of this work, let us mention a few interesting features. The generation of each of the 28 datasets in Table III typically requires computational times  $\simeq 0.1$  s, though for some configurations like #21, #27 and #28 it can reach up to  $\sim 0.25$  s because of the rather low starting frequency. The initial EOB frequencies  $\omega_a^{\text{EOB}}$  of Table III correspond, via  $GM_\odot/c^3 = 4.925490947 \times 10^{-6}$  s, to physical gravitational wave frequencies between  $\sim 11$  Hz and  $\sim 19$  Hz for a  $M = 50M_\odot$  binary. When attempting a preliminary parameter estimation run on GW150914, this yielded a total running time of approximately four days on a single Intel Xeon at 2.2GHz CPU with 32 cores. This paves the way to new, independent, estimates of eccentricity on LIGO-Virgo events [43–46, 46–49] via analytical waveform models, possibly not limited by the hypothesis of mild eccentricities.

### Acknowledgments

We are grateful to R. Gamba and M. Breschi preliminary tests of the performance of the  $C$  implementation on GW150914 data and for comments on the manuscript. A. N. is grateful to S. Albanesi and T. Damour for discussions, and especially to S. Bernuzzi for the daily exchange of ideas and for the music. We are grateful to D. Chiaramello for collaboration in the early stages of this project. We appreciate technical comments from I. Romero-Shaw and M. Zevin.

### Appendix A: Derivation of $\hat{\mathcal{F}}_r$ as used in Refs. [1, 2]

In Refs. [1, 2] it was used the general, non circularized, 2PN-accurate resummed form of the radial force  $\hat{\mathcal{F}}_r$ ,

whose expression was not written explicitly. The purpose of this Appendix is two fold: on the one hand, fill the information missing in previous literature; on the other hand, highlight that the action of  $\hat{\mathcal{F}}_r$  becomes unacceptably large in strong field and prevents us from exploiting in full the natural flexibility of the EOB  $A$  function through  $a_6^c(\nu)$  that has been key in previous EOB/NR works, e.g. [16, 17, 24, 25]. To overcome this difficulty, that we will discuss below, we decided to adopt the quasi-circular expression for  $\hat{\mathcal{F}}_r$  of Eq. (3) used in the main text. Before entering in the details of this issue, let us review the analytical steps that brought us to the expression of  $\hat{\mathcal{F}}_r$  used in Refs. [1, 2] Let us start by recalling the expression of  $\hat{\mathcal{F}}_r$  given in Eq. (3.70) of Ref. [20], that reads

$$\hat{\mathcal{F}}_r = \frac{p_r}{r^3} \left( \sum_{i=1}^4 T_i X^i + \epsilon^2 \sum_{i,j=1}^4 T_{ijk} X^{ij} + \epsilon^4 \sum_{i,j,k=1}^4 T_{ijk} X^{ijk} \right) \quad (\text{A1})$$

where  $\epsilon \equiv c^{-1}$  as a reminder of the explicit PN expansion at 2PN. The EOB scalars  $X_i$ , as introduced in Eqs. (3.17) and (3.41) of Ref. [20], read

$$X_1 = p^2, \quad (\text{A2})$$

$$X_2 = p_r^2, \quad (\text{A3})$$

$$X_3 = u \quad (\text{A4})$$

$$X_4 = r \partial_r \hat{H}_{\text{EOB}}, \quad (\text{A5})$$

where  $p \equiv \left( p_\varphi^2 u^2 + B^{-1} p_r^2 \right)^{1/2}$  and  $A$  e  $B$  are the EOB potentials and in the equation above we introduced the shorthands  $X_{ij} \equiv X_i X_j$  and  $X_{ijk} \equiv X_i X_j X_k$ . The  $(T_i T_{ij}, T_{ijk})$  are expressed in Eqs. (D9-D11) of Ref. [20]

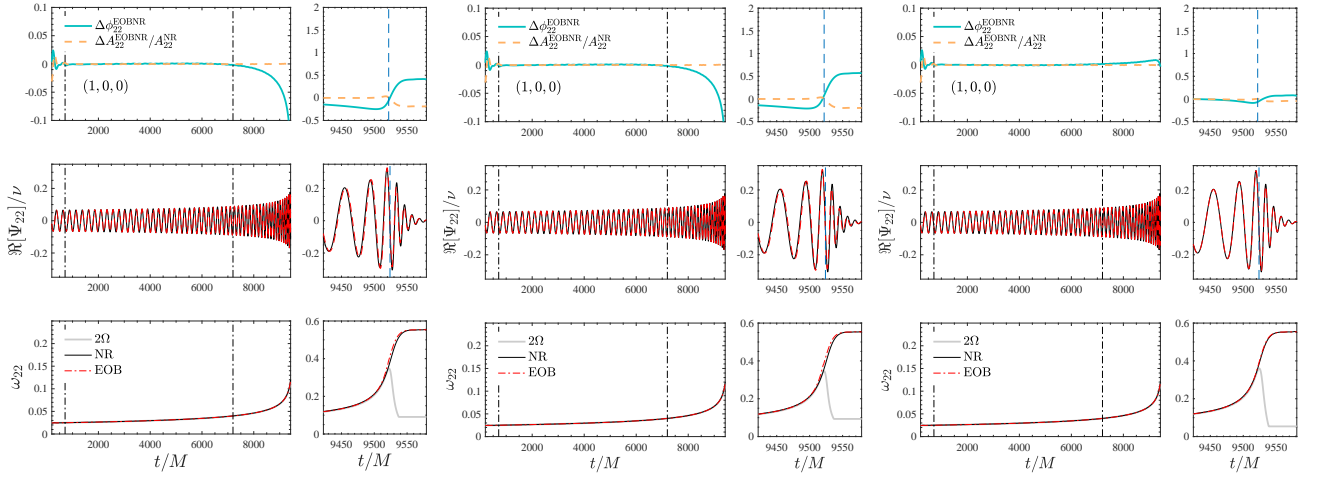


FIG. 17: Left panel: EOB/NR phasing comparison for  $q = 1$ , with the quasi-circular  $\hat{\mathcal{F}}_r$  and  $a_6^c = 281.62$ , Eq. (6). Middle panel: same comparison, with the same value of  $a_6^c = 281.62$ , but using the general expression of  $\hat{\mathcal{F}}_r$  given by the resummed version of Eq. (A24). In this case one sees a slightly larger phase difference accumulated during plunge up to merger and ringdown. Right panel: phasing comparison with the standard, quasi-circular, **TEOBResumS** model [17].

and we report them here explicitly for convenience. The  $T_i$  read

$$T_2 = 0, \quad T_3 = \frac{32\nu}{3}, \quad T_4 = -\frac{56\nu}{5}. \quad (\text{A6})$$

The  $T_{ij}$  read

$$T_{22} = 0, \quad (\text{A7})$$

$$T_{23} = \nu \left( \frac{4\nu}{7} + \frac{100}{21} \right), \quad (\text{A8})$$

$$T_{24} = \nu \left( -\frac{76\nu}{105} - \frac{232}{105} \right), \quad (\text{A9})$$

$$T_{33} = \nu \left( -\frac{3776\nu}{105} - \frac{4532}{105} \right), \quad (\text{A10})$$

$$T_{34} = \nu \left( \frac{1172\nu}{35} + \frac{998}{105} \right), \quad (\text{A11})$$

$$T_{44} = \nu \left( \frac{368}{21} - \frac{400\nu}{21} \right). \quad (\text{A12})$$

$$T_{222} = 0, \quad (\text{A13})$$

$$T_{223} = \nu \left( -\frac{206\nu^2}{315} - \frac{94\nu}{35} - \frac{14}{15} \right), \quad (\text{A14})$$

$$T_{224} = \nu \left( \frac{88\nu^2}{189} + \frac{1382\nu}{945} + \frac{1088}{945} \right), \quad (\text{A15})$$

$$T_{233} = \nu \left( -\frac{1312\nu^2}{2835} - \frac{17678\nu}{567} - \frac{1024}{135} \right), \quad (\text{A16})$$

$$T_{234} = \nu \left( -\frac{263\nu^2}{945} + \frac{550\nu}{27} + \frac{209}{21} \right), \quad (\text{A17})$$

$$T_{244} = \nu \left( \frac{104\nu^2}{315} - \frac{1786\nu}{315} + \frac{562}{315} \right), \quad (\text{A18})$$

$$T_{333} = \nu \left( \frac{1748\nu^2}{35} + \frac{1138\nu}{5} - \frac{351098}{2835} \right), \quad (\text{A19})$$

$$T_{334} = \nu \left( -\frac{73384\nu^2}{945} - \frac{63173\nu}{945} + \frac{16148}{189} \right), \quad (\text{A20})$$

$$T_{344} = \nu \left( \frac{7544\nu^2}{135} - \frac{5584\nu}{315} - \frac{33976}{945} \right), \quad (\text{A21})$$

$$T_{444} = \nu \left( -\frac{836\nu^2}{105} + \frac{5393\nu}{315} - \frac{968}{315} \right). \quad (\text{A22})$$

Then, the  $X_4$  we use in practice is given by Eq. (A5) expanded at 2PN accuracy, and similarly  $X_1$  at 2PN reads (see Eq. (3.47) of Ref. [20])

$$\begin{aligned} X_1 = & X_2 + X_3 - X_4 + \epsilon^2 \left( 2X_{23} - \frac{1}{2}(\nu+1)X_{24} + 3X_{33} \right. \\ & + \frac{1}{2}(\nu-5)X_{34} + \frac{1}{2}(\nu+1)X_{44} \Big) + \epsilon^4 \left( \frac{1}{8}(\nu^2 - \nu + 1)X_{224} \right. \\ & + (2-6\nu)X_{233} - \frac{1}{4}(\nu^2 + \nu + 3)X_{234} + \frac{3\nu}{4}X_{244} \\ & - 3(\nu-3)X_{333} + \frac{1}{8}(\nu^2 + 7\nu - 63)X_{334} + \frac{1}{4}(5\nu+8)X_{344} \\ & \left. - \frac{1}{8}(\nu^2 + 5\nu + 1)X_{444} \right). \end{aligned} \quad (\text{A23})$$

As a last step, we replace the radial momentum  $p_r$  with  $p_{r*}$  using the usual relation  $p_r = p_{r*} \sqrt{B/A}$  at 2PN so that we finally obtain (setting  $\epsilon = 1$ )

$$\hat{\mathcal{F}}_r = \nu p_{r*} u^4 (\hat{f}_r^N + \hat{f}_r^{1\text{PN}} + \hat{f}_r^{2\text{PN}}), \quad (\text{A24})$$

where

$$\hat{f}_r^N = -\frac{8}{15} + \frac{56}{5} p_\varphi^2 u, \quad (\text{A25})$$

$$\begin{aligned}
\hat{f}_r^{\text{1PN}} = & \left( \frac{556\nu}{105} - \frac{1228}{105} \right) p_{r*}^2 + \left( \frac{16\nu}{21} - \frac{1984}{105} \right) u \\
& + \left( -\frac{436\nu}{105} - \frac{124}{105} \right) p_{r*}^2 p_\phi^2 u \\
& + \left( \frac{1252}{105} - \frac{2588\nu}{105} \right) p_\phi^4 u^3 \\
& + \left( -\frac{1268\nu}{105} - \frac{1696}{35} \right) p_\phi^2 u^2, \quad (\text{A26})
\end{aligned}$$

$$\begin{aligned}
\hat{f}_r^{\text{2PN}} = & \left( -\frac{1273\nu^2}{315} + \frac{1061\nu}{315} + \frac{323}{315} \right) p_{r*}^4 \\
& + \left( -\frac{3548\nu^2}{315} + \frac{9854\nu}{105} + \frac{59554}{2835} \right) u^2 \\
& + \left( -\frac{8804\nu^2}{315} + \frac{10292\nu}{315} - \frac{1774}{21} \right) p_{r*}^2 p_\phi^2 u^2 \\
& + \left( \frac{194\nu^2}{7} - \frac{1052\nu}{105} - \frac{628}{105} \right) p_{r*}^2 p_\phi^4 u^3 \\
& + \left( -\frac{1752\nu^2}{35} + \frac{9568\nu}{315} - \frac{29438}{315} \right) p_\phi^2 u^3 \\
& + \left( \frac{131\nu^2}{63} - \frac{983\nu}{315} - \frac{461}{315} \right) p_{r*}^4 p_\phi^2 u \\
& + \left( -\frac{218\nu^2}{189} + \frac{17590\nu}{189} + \frac{20666}{315} \right) p_{r*}^2 u \\
& + \left( \frac{3277\nu^2}{105} - \frac{718\nu}{63} - \frac{3229}{315} \right) p_\phi^6 u^5 + \quad (\text{A27}) \\
& + \left( \frac{25217\nu^2}{315} + \frac{1606\nu}{15} - \frac{35209}{315} \right) p_\phi^4 u^4.
\end{aligned}$$

The function  $\tilde{\mathcal{F}}_r^{\text{2PN}} \equiv \hat{f}_r^{\text{N}} + \hat{f}_r^{\text{1PN}} + \hat{f}_r^{\text{2PN}}$  is then written as  $\tilde{\mathcal{F}}_r^{\text{2PN}} = \hat{f}_r^{\text{N}} \tilde{f}_r$ , where  $\tilde{f}_r \equiv 1 + c^{\text{1PN}} u + c_{\text{2PN}} u^2$ , and  $c^{\text{1PN,2PN}} \equiv \hat{f}_r^{\text{1PN,2PN}} / \hat{f}_r^{\text{N}}$ , and it is then resummed using a (0, 2) Padé approximant. This is the prescription of  $\hat{\mathcal{F}}_r$  used in previous<sup>14</sup> works [1, 2]. As mentioned in the main text, we realized that such expression becomes too large in strong field and prevents us to efficiently inform  $a_6^c(\nu)$  so to obtain an acceptably small EOB/NR phase difference up to merger. In particular, one realizes that the dynamics becomes practically insensitive to  $a_6^c$ , so that it is necessary to increase it a lot to gain minimal improvements around merger. In particular this implies large differences between the best value for  $q = 1$  and the best value for  $q = 2$ . This effect, though still there,

TABLE V: Maximal values of unfaithfulness for spinning datasets with  $q = 1$ . From left to right, the columns report: the number of dataset; the SXS simulation number; mass ratio and dimensionless spins  $(q, \chi_1, \chi_2)$ ; the maximum value of the unfaithfulness  $\bar{F}_{\text{NR/NR}}^{\text{max}}$  taken between the two highest NR resolutions, see Ref. [17], and and between EOB and NR waveforms,  $\bar{F}_{\text{EOB/NR}}^{\text{max}}$ , see Fig. 3.

#	id	$(q, \chi_1, \chi_2)$	$\bar{F}_{\text{NR/NR}}^{\text{max}}[\%]$	$\bar{F}_{\text{EOB/NR}}^{\text{max}}[\%]$
1	BBH:0180	(1, 0, 0)	0.0035	0.65
2	BBH:0007	(1.5, 0, 0)	0.0020	0.40
3	BBH:0169	(2, 0, 0)	0.0032	0.19
4	BBH:1221	(3, 0, 0)	0.0016	0.14
5	BBH:0294	(3.5, 0, 0)	0.0102	0.066
6	BBH:0167	(4, 0, 0)	0.0057	0.082
7	BBH:0056	(5, 0, 0)	0.0158	0.058
8	BBH:0166	(6, 0, 0)	..	0.057
9	BBH:0063	(8, 0, 0)	0.0754	0.056
10	BBH:0303	(10, 0, 0)	0.0045	0.059
11	BBH:1124	(1, +0.998, +0.998)	...	0.18
12	BBH:0178	(1, +0.9942, +0.9942)	0.0066	0.23
13	BBH:0177	(1, +0.9893, +0.9893)	0.0021	0.15
14	BBH:0172	(1, +0.9794, +0.98)	0.0022	0.21
15	BBH:0158	(1, +0.97, +0.97)	0.31	0.25
16	BBH:0157	(1, +0.95, +0.95)	0.0027	0.20
17	BBH:0160	(1, +0.9, +0.9)	0.0118	0.48
18	BBH:0153	(1, +0.85, +0.85)	..	0.61
19	BBH:0230	(1, +0.8, +0.8)	0.0016	0.63
20	BBH:0228	(1, +0.6, +0.6)	0.0080	0.62
21	BBH:1122	(1, +0.44, +0.44)	0.0031	0.62
22	BBH:0150	(1, +0.2, +0.2)	0.0027	0.86
23	BBH:0149	(1, -0.2, -0.2)	0.0037	0.63
24	BBH:0148	(1, -0.44, -0.44)	0.0013	0.38
25	BBH:0215	(1, -0.6, -0.6)	0.0040	0.22
26	BBH:0154	(1, -0.8, -0.8)	0.0036	0.19
27	BBH:0159	(1, -0.9, -0.9)	0.0069	0.20
28	BBH:0156	(1, -0.95, -0.95)	0.0055	0.23
29	BBH:0156	(1, -0.97, -0.97)	0.0055	0.24
30	BBH:0231	(1, +0.9, 0)	0.0046	1.00
31	BBH:0232	(1, +0.9, +0.5)	0.0073	1.19
32	BBH:0224	(1, +0.40, -0.80)	0.002	0.29

is less dramatic with the quasi-circular expression, that allows one to obtain more easily a good EOB/NR phasing agreement through plunge, merger and ringdown. To get a more precise understanding of the effect we report in Fig. 17 three EOB/NR phasing comparisons. The left and middle panel of the figure are obtained with the eccentric model and both share the same value of  $a_6^c = 281.62$  but: (i) the leftmost panel uses the quasi-circular expression for  $\hat{\mathcal{F}}_r$  Eq. (6) instead of the general

<sup>14</sup> Note that due to a calculation error, the coefficients that now correctly read  $9854\nu/105$  and  $9568\nu/315$  were respectively replaced by  $9686\nu/105$  and  $58424\nu/315$  in Refs. [1, 2]. This does not have any meaningful impact on the results discussed therein.

TABLE VI: Maximal values of unfaithfulness for spinning datasets with  $q \neq 1$ . From left to right, the columns report: the number of dataset; the SXS simulation number; mass ratio and dimensionless spins  $(q, \chi_1, \chi_2)$ ; the maximum value of the unfaithfulness  $\bar{F}_{\text{NR/NR}}^{\text{max}}$  taken between the two highest NR resolutions, see Ref. [17], and between EOB and NR waveforms,  $\bar{F}_{\text{EOB/NR}}^{\text{max}}$ , see Fig. 3.

#	id	$(q, \chi_1, \chi_2)$	$\bar{F}_{\text{NR/NR}}^{\text{max}} [\%]$	$\bar{F}_{\text{EOB/NR}}^{\text{max}} [\%]$
33	BBH: 1146	(1.5, +0.95, +0.95)	...	0.23
34	BBH:0234	(2, -0.85, -0.85)	0.0049	0.16
35	BBH:0239	(2, -0.37, +0.85)	0.0005	0.13
36	BBH:0252	(2, +0.37, -0.85)	0.0029	0.44
37	BBH:0257	(2, +0.85, +0.85)	0.0024	0.070
38	BBH:0260	(3, -0.85, -0.85)	0.0004	0.12
39	BBH:0268	(3, -0.40, -0.60)	0.0016	0.13
40	BBH:0285	(3, +0.40, +0.60)	0.0013	0.36
41	BBH:0293	(3, +0.85, +0.85)	0.0046	0.013
42	BBH:1434	(4.368, +0.80, +0.80)	...	0.096
43	BBH:0208	(5, -0.90, 0)	0.0385	0.091
44	BBH:1463	(5, +0.61, 0.24)	0.0032	0.49
45	BBH:1432	(5.841, +0.66, 0.80)	0.0192	0.38
46	BBH:0207	(7, -0.60, 0)	0.011	0.059
47	BBH:0205	(7, -0.40, 0)	0.0040	0.062
48	BBH:0203	(7, +0.40, 0)	0.0095	0.23
49	BBH:0202	(7, +0.60, 0)	0.048	0.75
50	BBH:1375	(8, -0.90, 0)	...	0.22
51	BBH:1419	(8, -0.80, -0.80)	...	0.16
52	BBH:1426	(8, +0.48, +0.75)	0.0378	0.091
53	BAM	(8, +0.85, +0.85)	...	1.108

one discussed here and shown in the middle panel. In this second case, the figure highlights that a (slightly) larger phase difference accumulated during the late plunge up to merger and ringdown. Note that this difference cannot be reabsorbed by changing further (i.e., by increasing)  $a_6^c$ ; it is due to a  $\hat{\mathcal{F}}_r$  that, despite the resummation, keeps growing in strong field and dominates the dynamics in the very late plunge phase. For the sake of comparison, the right panel of Fig. 17 also shows the phasing agreement yielded by the standard, quasi-circular model `TEOBResumS` of Ref. [17] that has, by construction,  $\hat{\mathcal{F}}_r = 0$ . Although the phase disagreement shown in the figure has little impact, in terms of  $\bar{F}_{\text{EOB/NR}}$ , for such an equal-mass, nonspinning binary, it becomes unacceptably larger when spin is switched on. For example, we have verified that a model constructed with the general (resummed)  $\hat{\mathcal{F}}_r$  leads to  $\bar{F}_{\text{EOB/NR}}^{\text{max}} \simeq 4\%$  for a quasi-circular configuration with  $(q, \chi_1, \chi_2) = (1, +0.95, +0.95)$ , and this difference cannot be cured neither changing  $a_6^c$ , nor  $c_3$ , because it is fundamentally due to  $\hat{\mathcal{F}}_r$ . At the moment, the choice of the 2PN-resummed quasi-circular ex-

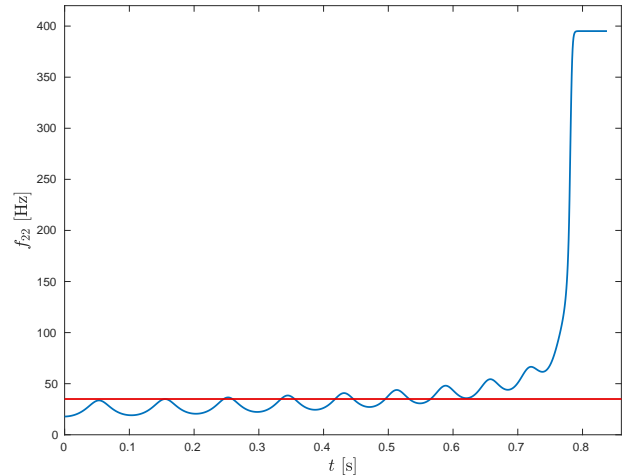


FIG. 18: Gravitational wave frequency  $f_{22}$  of the  $\ell = m = 2$  mode of signal generated with `TEOBResumSGeneral` using  $M = 45M_\odot$ ,  $q = 1.24138$ ,  $\chi_{1,2} = 0$ ,  $D_L = 410$ ,  $\iota = 1.309$ ,  $e_{\omega_0}^{\text{EOB}} = 0.2$  and initial frequency at periastron equal to 35 Hz (red line). Changing the prescription for the initial frequency of 35 Hz would approximately mean starting the system at the apastron around  $t = 0.62$  s when using  $\omega_a^{\text{EOB}}$  or around  $t = 0.47$  s for  $\omega_{\text{secular}}^{\text{EOB}}$ .

pression of  $\hat{\mathcal{F}}_r$  seems to give an acceptable compromise to get the model consistent in terms of losses as well as accurate versus quasi-circular NR simulations.

## Appendix B: Explicit EOB/NR unfaithfulness results

In this Appendix we list the explicit values of the maximum EOB/NR unfaithfulness  $\bar{F}_{\text{EOB/NR}}^{\text{max}}$  on the meaningful portion of the SXS catalog that we considered to obtain Fig. 3. The data are listed in Table V, for non-spinning and equal mass, spinning configurations, and in Table VI for unequal mass, spinning configurations.

## Appendix C: `TEOBResumSGeneral` C code

The EOB waveform model `TEOBResumSGeneral` discussed in this paper is publicly available as a stand-alone C implementation via a `bitbucket` git repository [42]. It can deal with quasi-circular configuration, eccentric inspirals or hyperbolic encounters. As discussed in the main text, an eccentric waveform is computed by specifying an initial GW frequency  $\omega_0^{\text{EOB}}$  and a corresponding value of the EOB eccentricity at this frequency  $e_{\omega_0}^{\text{EOB}}$ . It is convenient to start the system specifying the initial apastron frequency  $\omega_a^{\text{EOB}}$ , posing  $\omega_0^{\text{EOB}} = \omega_a^{\text{EOB}}$ . However, to maintain continuity with respect to the circular waveforms, the initial conditions can also be determined using the starting secular (i.e. average of the apastron and periastron) frequency  $\omega_{\text{secular}}^{\text{EOB}}$ . The difference be-



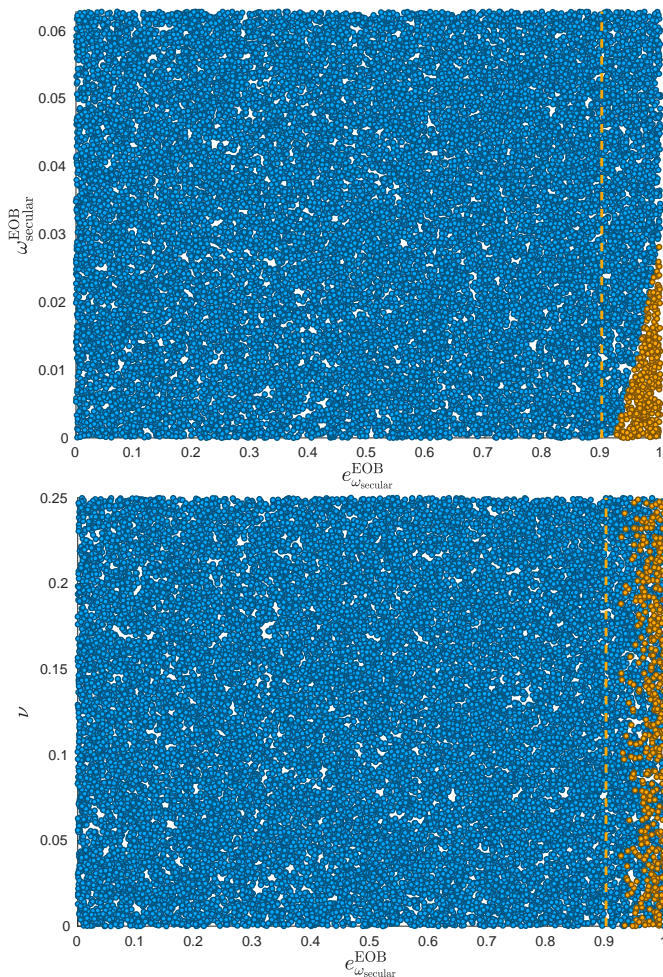


FIG. 19: Reliability of waveform generation over the parameter space for eccentric inspirals. The markers in the plot correspond to waveforms generated with the **TEOBResumSGeneral** code, specifying the initial secular frequency,  $\omega_{\text{secular}}^{\text{EOB}}$  and the corresponding eccentricity  $e_{\text{secular}}^{\text{EOB}}$ . We here show 25000 points, with parameters randomly generated in the ranges:  $\nu \in (0, 0.25)$ ,  $(\chi_1, \chi_2) \in (-1, +1)$ ;  $\omega_{\text{secular}}^{\text{EOB}} \in (0, 10^{-2}) \times 2\pi$ ;  $e_{\text{secular}}^{\text{EOB}} \in (0, 1)$ . Blue dots mark successfully computed waveforms, while orange dots mark configurations for which the initial conditions could not be generated. The dashed orange line corresponds to  $e_{\text{secular}}^{\text{EOB}} = 0.9$ .

tween these two approaches is clarified in Fig. 18.

Using frequency and eccentricity as initial conditions, extending the usual prescription for circular systems, **TEOBResumSGeneral** can reliably generate waveforms with eccentricity  $e_0^{\text{EOB}} \lesssim 0.9$ , see Fig. 19. For higher eccentricities, this approach fails to correctly compute initial conditions. Its region of validity could be extended, but it will inexorably fail somewhere near the limit  $e \rightarrow 1$ , i.e. near head-on collisions. A more robust procedure, in this case, is to initiate the dynamics specifying values of the energy and angular momentum, coherently with

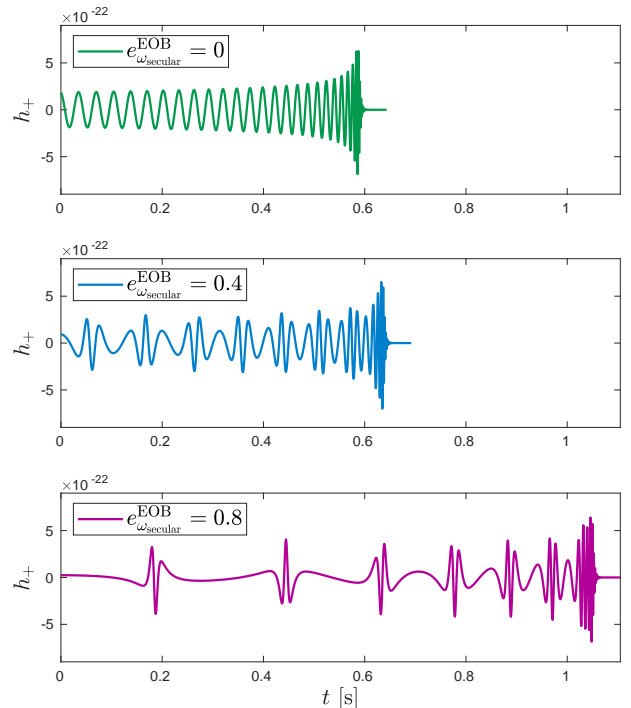


FIG. 20: Visual comparison of GW signals with different initial eccentricities. The waveforms are generated with **TEOBResumSGeneral** using  $M = 45M_\odot$ ,  $q = 1.24138$ ,  $\chi_i = 0$ ,  $D_L = 410$ ,  $\iota = 1.309$ ,  $\omega_{\text{secular}}^{\text{EOB}} = 35 \times 2\pi$  Hz and  $e_{\text{secular}}^{\text{EOB}} = (0, 0.4, 0.8)$ .

what is done for hyperbolic systems [2], but selecting stable configurations. We also point out that, while the model could not be validated with NR simulations, it still produces sane waveforms also for extreme values of the eccentricity. An example is shown in Fig. 20, that illustrates three cases of (nonspinning) waveforms starting at the same secular frequency but with eccentricities  $e_{\text{secular}}^{\text{EOB}} = (0, 0.4, 0.8)$ . Note, in the third case, that, despite the sequence of short-duration bursts, the system essentially circularizes before merger and ringdown.

A detailed study of computation times is shown in Fig. 21. The bottom panel of the figure selects mass ratio  $q < 50$ , so to have an estimate of the timing needed for generating waveforms consistent with the currently published LIGO-Virgo events [50]. As mentioned in the main text, our implementation is sufficiently efficient to be used for inferring eccentricity measurements at least from GW150914-like events. To do so, one needs to consider *both*  $(\omega_{\text{EOB}}^{\text{secular}}, e_{\text{EOB}}^{\text{secular}})$  as sampling parameters. This is necessary because the initial mean EOB anomaly is always set to zero, since the evolution of the system begins at the apastron. Therefore, in order to cover all possible configurations and avoid biases [51], the sampling of the mean anomaly typical of other approaches is replaced by the sampling of  $\omega_{\text{EOB}}^{\text{secular}}$ .

Finally, let us comment on extreme mass-ratio inspirals (EMRIs), given their importance for future space-based detectors such as LISA [52]. The generation time for

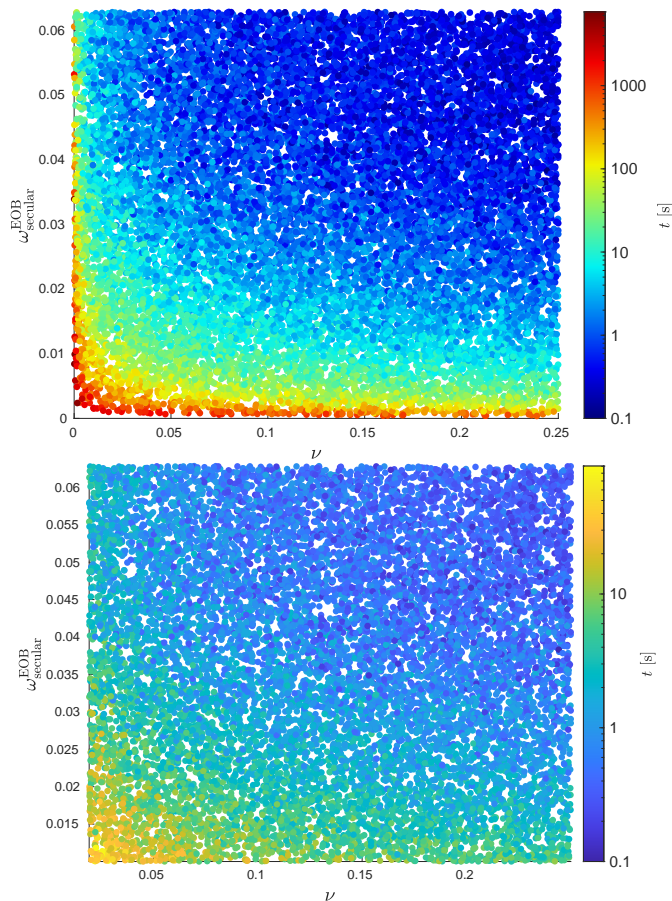


FIG. 21: Generation time analysis for TEOBResumSGeneral. Top panel. Timing of 25000 configurations, with parameters randomly generated in the same ranges as in Fig. 19. The color code indicates the computation time of each waveform in the time domain without interpolation on a uniformly spaced temporal grid. We omitted systems for which we could not compute the computation time. This can be due to the failure of the initial data prescription (equivalent to orange points in Fig. 19) or because the chosen configuration does not reach the merger before a time  $t/M = 10^9$  (very low starting frequency or very high mass ratio). Bottom panel: close-up on the region with  $q < 50$  and  $\omega_{\text{secular}}^{\text{EOB}} > 0.01$ , the part of parameter space that is of interest for currently published LIGO-Virgo events [50].

a one-year long EMRI ( $M = 10^6 M_{\odot}$ ,  $q = 10^5$ ) varies a lot depending on starting frequency and eccentricity. Let us consider as test case a nonspinning system with initial eccentricity  $e_{\text{EOB}}^{\text{secular}} = 0.3$ . The code takes around 30 seconds to generate a one-year long waveform when starting at a rather low frequency ( $\sim 10^{-4}$  Hz). The time increases to about 5 minutes when considering a higher starting frequency ( $\sim 10^{-3}$  Hz) and hence a phase in which the system is no longer adiabatic but instead it is slowly inspiralling.

- 
- [1] D. Chiamello and A. Nagar, Phys. Rev. D **101**, 101501 (2020), 2001.11736.
  - [2] A. Nagar, P. Retegno, R. Gamba, and S. Bernuzzi, Phys. Rev. D **103**, 064013 (2021), 2009.12857.
  - [3] T. Chu, H. P. Pfeiffer, and M. A. Scheel, Phys. Rev. D **80**, 124051 (2009), 0909.1313.
  - [4] G. Lovelace, M. Scheel, and B. Szilagyi, Phys. Rev. D **83**, 024010 (2011), 1010.2777.
  - [5] G. Lovelace, M. Boyle, M. A. Scheel, and B. Szilagyi, Class. Quant. Grav. **29**, 045003 (2012), 1110.2229.
  - [6] L. T. Buchman, H. P. Pfeiffer, M. A. Scheel, and B. Szilagyi, Phys. Rev. D **86**, 084033 (2012), 1206.3015.
  - [7] D. A. Hemberger, G. Lovelace, T. J. Loredo, L. E. Kidder, M. A. Scheel, B. Szilagyi, N. W. Taylor, and S. A. Teukolsky, Phys. Rev. D **88**, 064014 (2013), 1305.5991.
  - [8] M. A. Scheel, M. Giesler, D. A. Hemberger, G. Lovelace, K. Kuper, M. Boyle, B. Szilagyi, and L. E. Kidder, Class. Quant. Grav. **32**, 105009 (2015), 1412.1803.
  - [9] J. Blackman, S. E. Field, C. R. Galley, B. Szilagyi, M. A. Scheel, M. Tiglio, and D. A. Hemberger, Phys. Rev. Lett. **115**, 121102 (2015), 1502.07758.
  - [10] G. Lovelace et al., Class. Quant. Grav. **32**, 065007 (2015), 1411.7297.
  - [11] A. H. Mroue, M. A. Scheel, B. Szilagyi, H. P. Pfeiffer,

- fer, M. Boyle, et al., Phys.Rev.Lett. **111**, 241104 (2013), 1304.6077.
- [12] P. Kumar, K. Barkett, S. Bhagwat, N. Afshari, D. A. Brown, G. Lovelace, M. A. Scheel, and B. Szilágyi, Phys. Rev. **D92**, 102001 (2015), 1507.00103.
- [13] T. Chu, H. Fong, P. Kumar, H. P. Pfeiffer, M. Boyle, D. A. Hemberger, L. E. Kidder, M. A. Scheel, and B. Szilágyi, Class. Quant. Grav. **33**, 165001 (2016), 1512.06800.
- [14] M. Boyle et al., Class. Quant. Grav. **36**, 195006 (2019), 1904.04831.
- [15] SXS Gravitational Waveform Database, <https://data.black-holes.org/waveforms/index.html>.
- [16] A. Nagar, G. Pratten, G. Riemenschneider, and R. Gamba (2019), 1904.09550.
- [17] A. Nagar, G. Riemenschneider, G. Pratten, P. Rettengo, and F. Messina (2020), 2001.09082.
- [18] A. Nagar et al., Phys. Rev. **D98**, 104052 (2018), 1806.01772.
- [19] T. Damour and A. Nagar, Phys.Rev. **D90**, 044018 (2014), 1406.6913.
- [20] D. Bini and T. Damour, Phys.Rev. **D86**, 124012 (2012), 1210.2834.
- [21] T. Damour, B. R. Iyer, and A. Nagar, Phys. Rev. **D79**, 064004 (2009), 0811.2069.
- [22] T. Damour and A. Gopakumar, Phys. Rev. **D73**, 124006 (2006), gr-qc/0602117.
- [23] T. Damour and A. Nagar, Phys. Rev. **D77**, 024043 (2008), 0711.2628.
- [24] A. Nagar, G. Riemenschneider, and G. Pratten, Phys. Rev. **D96**, 084045 (2017), 1703.06814.
- [25] P. Rettengo, F. Martinetti, A. Nagar, D. Bini, G. Riemenschneider, and T. Damour (2019), 1911.10818.
- [26] Updated Advanced LIGO sensitivity design curve, <https://dcc.ligo.org/LIGO-T1800044/public>.
- [27] L. London, D. Shoemaker, and J. Healy, Phys. Rev. **D90**, 124032 (2014), [Erratum: Phys. Rev.D94,no.6,069902(2016)], 1404.3197.
- [28] A. Taracchini, A. Buonanno, G. Khanna, and S. A. Hughes, Phys.Rev. **D90**, 084025 (2014), 1404.1819.
- [29] L. London and E. Fauchon-Jones, Class. Quant. Grav. **36**, 235015 (2019), 1810.03550.
- [30] I. Hinder, L. E. Kidder, and H. P. Pfeiffer (2017), 1709.02007.
- [31] A. Ramos-Buades, S. Husa, G. Pratten, H. Estellés, C. García-Quirós, M. Mateu, M. Colleoni, and R. Jaume (2019), 1909.11011.
- [32] M. Zilhão and F. Löffler, Int. J. Mod. Phys. A **28**, 1340014 (2013), 1305.5299.
- [33] D. Shoemaker, <https://dcc.ligo.org/cgi-bin/DocDB/ShowDocument?docid=2974>, URL <https://dcc.ligo.org/cgi-bin/DocDB/ShowDocument?docid=2974>.
- [34] T. Hinderer and S. Babak, Phys. Rev. **D96**, 104048 (2017), 1707.08426.
- [35] T. Damour, A. Nagar, and S. Bernuzzi, Phys.Rev. **D87**, 084035 (2013), 1212.4357.
- [36] C. K. Mishra, K. G. Arun, and B. R. Iyer, Phys. Rev. **D91**, 084040 (2015), 1501.07096.
- [37] M. Ebersold, Y. Boetzel, G. Faye, C. K. Mishra, B. R. Iyer, and P. Jetzer, Phys. Rev. D **100**, 084043 (2019), 1906.06263.
- [38] N. Loutrel (2020), 2009.11332.
- [39] N. Loutrel, Class. Quant. Grav. **38**, 015005 (2021), 2003.13673.
- [40] S. Mukherjee, S. Mitra, and S. Chatterjee (2020), 2010.00916.
- [41] T. Damour, F. Guercilena, I. Hinder, S. Hopper, A. Nagar, et al. (2014), 1402.7307.
- [42] [https://bitbucket.org/eob\\_ihes/teobresums/src/master/](https://bitbucket.org/eob_ihes/teobresums/src/master/), TEOBResumS code.
- [43] X. Liu, Z. Cao, and L. Shao (2019), 1910.00784.
- [44] M. E. Lower, E. Thrane, P. D. Lasky, and R. Smith, Phys. Rev. D **98**, 083028 (2018), 1806.05350.
- [45] I. M. Romero-Shaw, P. D. Lasky, and E. Thrane, Mon. Not. Roy. Astron. Soc. **490**, 5210 (2019), 1909.05466.
- [46] I. M. Romero-Shaw, P. D. Lasky, E. Thrane, and J. C. Bustillo (2020), 2009.04771.
- [47] J. CalderF3n Bustillo, N. Sanchis-Gual, A. Torres-FornE9, and J. A. Font (2020), 2009.01066.
- [48] J. Calderón Bustillo, N. Sanchis-Gual, A. Torres-Forné, J. A. Font, A. Vajpeyi, R. Smith, C. Herdeiro, E. Radu, and S. H. W. Leong (2020), 2009.05376.
- [49] V. Gayathri, J. Healy, J. Lange, B. O’Brien, M. Szczepanczyk, I. Bartos, M. Campanelli, S. Klimenko, C. Lousto, and R. O’Shaughnessy (2020), 2009.05461.
- [50] R. Abbott et al. (LIGO Scientific, Virgo) (2020), 2010.14527.
- [51] T. Islam, V. Varma, J. Lodman, S. E. Field, G. Khanna, M. A. Scheel, H. P. Pfeiffer, D. Gerosa, and L. E. Kidder, Phys. Rev. D **103**, 064022 (2021), 2101.11798.
- [52] P. Amaro-Seoane et al. (LISA) (2017), 1702.00786.